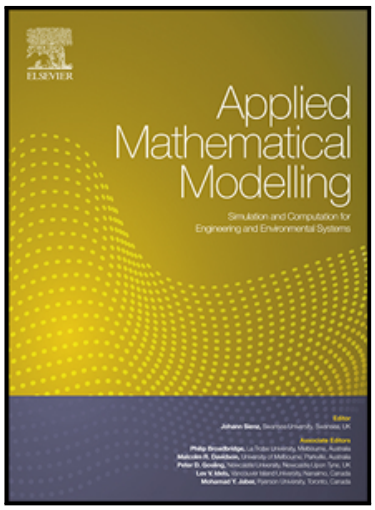

Modelling reservoir sediment flushing through a bottom tunnel with an initially covered intake

Yining Sun , Ji Li , Zhixian Cao , Jinxin Liu , Huan Xu , Alistair G.L. Borthwick

PII: S0307-904X(23)00458-4
DOI: https://doi.org/10.1016/j.apm.2023.10.018
Reference: APM 15231

To appear in: *Applied Mathematical Modelling*

Received date: 15 April 2023
Revised date: 2 October 2023
Accepted date: 5 October 2023

Please cite this article as: Yining Sun , Ji Li , Zhixian Cao , Jinxin Liu , Huan Xu , Alistair G.L. Borthwick , Modelling reservoir sediment flushing through a bottom tunnel with an initially covered intake, *Applied Mathematical Modelling* (2023), doi: https://doi.org/10.1016/j.apm.2023.10.018

Highlights

- A coupled model is proposed integrating a 2D double layer-averaged model for reservoir and a 1D model for bottom tunnel
- High water level, small cover layer thickness, short tunnel length and steep tunnel slope favour the occurrence of sediment flushing
- Low water level, large cover layer thickness, long tunnel length and gentle tunnel slope are more likely to cause tunnel blockage

Modelling reservoir sediment flushing through a bottom tunnel with an initially covered intake

Yining Sun[a], Ji Li[b], Zhixian Cao[a*], Jinxin Liu[c], Huan Xu[a] and Alistair G.L. Borthwick[d,e]

a State Key Laboratory of Water Resources and Hydropower Engineering Science, Wuhan University, Wuhan 430072, China

b Zienkiewicz Centre for Computational Engineering, Faculty of Science and Engineering, Swansea University, Swansea SA1 8EN, UK

c Changjiang Survey, Planning, Design and Research, Co., Ltd., Wuhan, 430010, China

d Institute for Infrastructure and Environment, University of Edinburgh, Edinburgh EH9 3JL, UK

e School of Engineering, Computing and Mathematics, University of Plymouth, Plymouth PL4 8AA, UK

Correspondence

* Zhixian Cao, State Key Laboratory of Water Resources and Hydropower Engineering Science, Wuhan University, Wuhan 430072, China. E-mail: zxcao@whu.edu.cn

ABSTRACT

Sediment flushing through a bottom tunnel is one of the most effective methods to alleviate reservoir sedimentation. However, the multi-physical hydro-sediment-morphological processes of reservoir sediment flushing through an initially covered bottom tunnel intake have remained poorly understood, and a physically enhanced and practically viable mathematical model is required. The present study uses an integrated model to resolve sediment flushing through an initially covered bottom tunnel intake. The proposed model couples a two-dimensional double layer-averaged model for the reservoir with a one-dimensional model for the bottom tunnel by means of numerical fluxes calculations at the inner boundary. The governing equations are solved synchronously using a well-balanced finite volume method. Several parameters related to boundary resistances and sediment exchange fluxes need to be determined for model closure. The model is tested against data from a series of physical experiments on reservoir sediment flushing, with sound agreement achieved between computed and measured scour hole geometries. Moreover, the present model successfully predicts the occurrence of tunnel blockage. The results prove that reservoir sediment flushing is best accomplished for high reservoir water level, small cover layer thickness, short tunnel length and steep tunnel slope. The present model facilitates reservoir design and operation to help preserve reservoir capacity.

KEYWORDS

Reservoir sedimentation; Bottom tunnel; Sediment flushing; Tunnel blockage; Double layer-averaged model

1 Introduction

Reservoirs on sandy rivers generally suffer excessive sedimentation [1, 2], which impinges on reservoir operation capacity and eventually leads to complete loss of functionality [3, 4]. Therefore, attention needs to be paid to reservoir sedimentation control [5-8], for which many strategies are commonly adopted [9-13]. Among these strategies, the present study focuses on sediment flushing, which is particularly effective at preserving long-term reservoir storage by utilizing water pressure to wash previously deposited sediment through bottom tunnels [5, 14].

Sediment flushing is typically induced by opening the sluice gate of bottom tunnels, with associated water level drawdown and regressive erosion in the reservoir, followed by jetting of highly concentrated water-sediment mixtures through bottom tunnels [13]. Over recent decades, numerous studies including laboratory-scale experiments [15-19] and numerical modelling [20-24] have focused on improving the efficiency of sediment flushing operations. Unfortunately, most previous studies were based on the precondition that sediment deposits near the bottom tunnel intake can be scoured and transported downstream on opening the tunnel gate. In fact, excess sediment deposits due to inappropriate operation or sudden hazards may be unable to be flushed out of the bottom tunnel, leading to tunnel blockage. There have been few systematic studies of this issue, the most notable by Xu et al. [25] who carried out a series of experiments on sediment flushing through bottom tunnels with initially covered intakes. Although empirical formulations for the geometry of the equilibrium funnel-shaped scour hole upstream of tunnel intake were proposed by Xu et al.

[25], the calculated threshold condition for the occurrence of sediment flushing was not sufficiently accurate due to limited data.

Numerical modelling offers a useful means of predicting the detailed process of reservoir sediment flushing. In cases involving initially covered bottom tunnels (intakes), both the open-channel flow in the reservoir and the pipe flow in the bottom tunnel must be resolved.

For reservoir flow, 1D (one-dimensional) (e.g., [26, 27]) models are inherently unable to simulate the lateral spreading of the funnel-shaped scour hole near the tunnel intake. However, fully 3D (three-dimensional) models (e.g., [22, 28]) incur excessive computational overheads and therefore are not feasible for large-scale, long-duration simulations of a reservoir. By contrast, 2D (two-dimensional) models offer a compromise between computational expense and accuracy, and hence are more suitable for the simulation of reservoir sediment flushing. In practice, turbidity currents, a kind of sharply stratified sediment-laden flow, are highly desirable for flushing sediment as much as possible out of reservoirs [3]. As the present state-of-the-art, the coupled 2D double layer-averaged model proposed by Cao et al. [29] is capable of resolving the whole series of processes behind reservoir turbidity currents, from formation and propagation to recession. This model, along with its recent extended version, has recently been applied to resolve hyper-concentrated turbidity currents, landslide-generated waves, and barrier lake formation and breach processes [30-33]. However, all these models set their downstream boundary at the bottom tunnel intake with outflow discharge determined with the method of characteristics or

empirical orifice flow formulations. In this way, the hydro-sediment-morphological processes inside the bottom tunnel are ignored.

For the pipe flow in the bottom tunnel, several models have been developed recently to simulate unsteady flow and sediment transport processes in sewer channels [34, 35], generally using the Saint-Venant equations along with an Exner-based equation [36, 37]. Furthermore, most existing sewer models experience major limitations, through either neglecting mass exchange between flow and bed in the bottom tunnel [38] or assuming the sediment transport is equal to equilibrium capacity [36, 39]. Recently, Liu et al. [40] proposed a coupled non-capacity model 1D model for resolving the hydro-sediment-morphodynamic processes of sewer flushing. However, this model cannot resolve the complicated physics of hyper-concentrated flows, where interphase and particle-particle interactions prevail [41], that frequently occur during the riverbed collapse process once the gate of the bottom tunnel has been opened [25].

In short, existing mathematical models cannot resolve sediment flushing through bottom tunnels with initially covered intakes, where multi-physical, interactions occur between flow hydrodynamics, sediment transport, and bed evolution. The present study proposes a coupled model that integrates a 2D double layer-averaged model for the reservoir and a 1D model for the bottom tunnel, which resolves both the hyper-concentrated stratified sediment-laden flow in the reservoir and pressurized flow in the bottom tunnel during the reservoir sediment flushing phase. The model is tested against measured data from a series of physical test cases by Xu et al. [25] with initially covered tunnel intakes, and then used to

investigate the effects of major factors in reservoir sediment flushing, including reservoir water level, cover layer thickness, and bottom tunnel length and slope.

2 Mathematical model

During a reservoir sediment flushing event through a bottom tunnel with an initially covered intake, once the gate of the tunnel intake is opened, sediment deposits upstream of the intake immediately collapse and slide into the tunnel, producing a subaqueous, highly concentrated sediment-laden flow, which may display non-Newtonian characteristics. Meanwhile, pressurized sediment flushing occurs in the bottom tunnel, and so the feedback effect of significant bed deformation in the bottom tunnel on the reservoir sediment flushing should be considered, a phenomenon that has not been previously modelled. Therefore, in the present study, a coupled model is proposed that integrates a 2D double layer-averaged model for the reservoir with a 1D model for the bottom tunnel, explicitly incorporating flow stratification, non-Newtonian rheology, sediment transport and morphological evolution, and thus is generally applicable to modelling the hydro-sediment-morphological process induced by the hyper-concentrated turbidity current in the reservoir and pressurized sediment-laden flow in the bottom tunnel.

2.1 Reservoir module

To model water-sediment flow in the reservoir, we use an extended 2D double layer-averaged model with non-Newtonian rheology derived by Sun et al. [30] who modified an earlier model proposed by Cao et al. [29] and Li et al. [31]. The double layer-averaged mod-

el comprises: (i) an upper clear-water flow layer; (ii) a lower sediment-laden flow layer; and (iii) an erodible bed with vanishingly small velocity. The 2D continuity and momentum equations for the upper clear-water and lower sediment-laden flow layers, the mass conservation equation for sediment carried by the flow, and the mass conservation equation for bed sediment are written:

$$\frac{\partial \eta_w}{\partial t}+\frac{\partial h_w U_w}{\partial x}+\frac{\partial h_w V_w}{\partial y}=-E_w+\frac{\partial \eta_s}{\partial t} \tag{2.1}$$

$$\frac{\partial h_w U_w}{\partial t}+\frac{\partial}{\partial x}\left[h_w U_w^2+0.5g\left(\eta_w^2-2\eta_w\eta_s\right)\right]+\frac{\partial}{\partial y}\left(h_w U_w V_w\right)=-\frac{\tau_{wx}}{\rho_w}-g\eta_w\frac{\partial \eta_s}{\partial x}-E_w U_w \tag{2.2}$$

$$\frac{\partial h_w V_w}{\partial t}+\frac{\partial}{\partial x}\left(h_w U_w V_w\right)+\frac{\partial}{\partial y}\left[h_w V_w^2+0.5g\left(\eta_w^2-2\eta_w\eta_s\right)\right]=-\frac{\tau_{wy}}{\rho_w}-g\eta_w\frac{\partial \eta_s}{\partial y}-E_w V_w \tag{2.3}$$

$$\frac{\partial \eta_s}{\partial t}+\frac{\partial h_s U_s}{\partial x}+\frac{\partial h_s V_s}{\partial y}=E_w \tag{2.4}$$

$$\begin{aligned}\frac{\partial h_s U_s}{\partial t}+\frac{\partial}{\partial x}\left[h_s U_s^2+0.5g\left(\eta_s^2-2\eta_s z_b\right)\right]+\frac{\partial}{\partial y}\left(h_s U_s V_s\right)&=-g\eta_s\frac{\partial z_b}{\partial x}-\frac{\rho_w g}{\rho_c}h_s\frac{\partial h_w}{\partial x}\\ -\frac{\left(\rho_0-\rho_c\right)\left(E-D\right)U_s}{\left(1-p\right)\rho_c}+\frac{\left(\rho_s-\rho_w\right)c_s U_s E_w}{\rho_c}+\frac{\rho_w E_w U_w}{\rho_c}-\frac{\left(\rho_s-\rho_w\right)g h_s^2}{2\rho_c}\frac{\partial c_s}{\partial x}&\\ +\frac{\tau_{wx}}{\rho_c}-\frac{\tau_{Nx}}{\rho_c}-\frac{1}{\rho_c}\left[\left(\frac{\tau_Y}{\left|\gamma_x\right|}+\mu_Y\right)\gamma_x\right]_{z=z_b}&\end{aligned} \tag{2.5}$$

$$\begin{aligned}\frac{\partial h_s V_s}{\partial t}+\frac{\partial}{\partial x}\left(h_s U_s V_s\right)+\frac{\partial}{\partial y}\left[h_s V_s^2+0.5g\left(\eta_s^2-2\eta_s z_b\right)\right]&=-g\eta_s\frac{\partial z_b}{\partial y}-\frac{\rho_w g}{\rho_c}h_s\frac{\partial h_w}{\partial y}\\ -\frac{\left(\rho_0-\rho_c\right)\left(E-D\right)V_s}{\left(1-p\right)\rho_c}+\frac{\left(\rho_s-\rho_w\right)c_s V_s E_w}{\rho_c}+\frac{\rho_w E_w V_w}{\rho_c}-\frac{\left(\rho_s-\rho_w\right)g h_s^2}{2\rho_c}\frac{\partial c_s}{\partial y}&\\ +\frac{\tau_{wy}}{\rho_c}-\frac{\tau_{Ny}}{\rho_c}-\frac{1}{\rho_c}\left[\left(\frac{\tau_Y}{\left|\gamma_y\right|}+\mu_Y\right)\gamma_y\right]_{z=z_b}&\end{aligned} \tag{2.6}$$

$$\frac{\partial h_s c_s}{\partial t}+\frac{\partial h_s U_s c_s}{\partial x}+\frac{\partial h_s V_s c_s}{\partial y}=E-D \tag{2.7}$$

$$\frac{\partial z_b}{\partial t}=-\frac{E-D}{1-p} \tag{2.8}$$

where t is time; g is gravitational acceleration; x and y are horizontal coordinates; h_w

and h_s are the thicknesses of the upper clear-water flow layer and the lower sediment-laden flow layer; U_w and V_w are the clear-water flow layer-averaged velocity components in the *x*- and *y*-directions; U_s and V_s are the sediment-laden flow layer-averaged velocity components in the *x*- and *y*-directions; c_s is the volumetric sediment concentration; η_w is the water surface elevation above a fixed horizontal datum; η_s is the elevation of the inter-face between the clear-water layer and sediment-laden flow layer above the same datum; z_b is the bed elevation; p is the bed sediment porosity; ρ_w and ρ_s are densities of water and sediment, respectively; $\rho_c = \rho_w(1-c_s)+\rho_s c_s$ is the density of water-sediment mixture; $\rho_0 = \rho_w p + \rho_s(1-p)$ is the density of the saturated bed; τ_{wx} and τ_{wx} are the bottom shear stress components for the clear-water flow layer in the *x*- and *y*-directions; γ_x and γ_y are shear rate components in the *x*- and *y*-directions; E_w is the water entrainment flux across the interface between the two layers; E, D are the sediment entrainment flux and sediment deposition flux, respectively.

A rheological model is introduced that represents non-Newtonian fluid characteristics through the effective bed shear stress $\tau_{eff} = \tau_B + \tau_N$, where $\tau_{Nx} = \tau_{fbx} + \tau_{sbx}$ and $\tau_{Ny} = \tau_{fby} + \tau_{sby}$ represent boundary resistance components summed across the Newtonian fluid and solid phases in the *x*- and *y*-directions, and τ_B is the shear stress due to non-Newtonian rheology as follows:

$$\begin{cases} \tau_B = \left(\tau_Y + \mu_Y |\gamma|\right)\mathrm{sgn}(\gamma) & |\tau_B| > \tau_Y \\ \gamma = 0 & |\tau_B| \le \tau_Y \end{cases} \tag{2.9}$$

where τ_Y is the yield stress; μ_Y is the dynamic viscosity; and $\gamma = \dfrac{\partial u}{\partial z}$ is the shear rate.

A set of relations is introduced to close the model to determine boundary resistances,

water entrainment, and sediment exchange fluxes (see Subsection S1.1.1 of Text S1 in the Supporting Information for details). Specifically, the Coulomb friction law and Manning's equation are used to determine resistances for the solid and Newtonian fluid phases, respectively, following Li et al. [42]. When the sediment concentration is higher than the threshold concentration, the lower sediment-laden flow layer acts as a non-Newtonian fluid, and the yield stress τ_Y and fluid consistency μ_Y are determined from formulae proposed by Fei et al. [43]. The shear stress τ_w at the interface between the upper and lower layers is estimated using Manning's equation, following Cao et al. [29]. Water entrainment E_w at the interface is calculated from the Richardson number, following Parker et al. [44]. Hindered sediment settling velocity and near-bed concentration are considered in evaluating the sediment deposition flux D, using a relationship determined by Richardson and Zaki [45]. Making the common assumption that entrainment always occurs at the same rate as in the capacity regime, the bed sediment entrainment flux is computed from the near-bed capacity sediment concentration and settling velocity, and the capacity transport rate is calculated using the Wu formula [39].

The two hyperbolic systems of governing equations for the two layers are solved separately and synchronously. Each hyperbolic system is solved by a quasi well-balanced numerical algorithm involving drying and wetting, using a second-order accurate finite volume Godunov-type approach in conjunction with a Harten-Lax-van Leer contact wave (HLLC) approximate Riemann solver [46] on a fixed rectangular mesh. Assuming that bed deformation is entirely determined by local entrainment and deposition fluxes in accordance with a non-capacity model of sediment transport, Eq. (2.8) is solved separately from the

other equations. A detailed description of the numerical algorithm is given by Cao et al. [29].

Notably, for a bed layer over the tunnel intake, once the gate of the bottom tunnel is opened, the bed material collapses quickly because the bed slope is larger than the repose angle. According to the geo-failure method proposed by Hu et al. [47], two main steps are involved in satisfying mass conservation during simulation of this collapse process (see Subsection S1.1.2 of Text S1 in the Supporting Information for details). Firstly, collapsing areas are identified where the local bed slope exceeds the repose angle of 30°. Then, the collapsed sediment is able to enter the ambient flow and produce a highly concentrated turbidity flow. The collapsed sediment will deposit onto the bed if the sediment concentration exceeds the transport capacity, or otherwise be transported through the bottom tunnel.

2.2 Bottom tunnel module

The computational module for sediment-laden flow in the bottom tunnel is extended from that of Liu et al. [40]. The governing equations of the 1D depth-averaged model [40] are derived from fundamental conservation laws for shallow water-sediment flow dynamics, to give:

$$\frac{\partial A}{\partial t}+\frac{\partial Q}{\partial x}=\frac{b(E-D)}{1-p} \tag{2.10}$$

$$\frac{\partial Q}{\partial t}+\frac{\partial}{\partial x}\left(\frac{Q^2}{A}+gI\right)=gAS_0-\frac{\tau_{eff}}{\rho}-gI\frac{(\rho_s-\rho_w)}{\rho}\frac{\partial c_s}{\partial x}+\frac{u\left(\rho_0-\rho\right)}{\rho}\frac{(D-E)b}{1-p} \tag{2.11}$$

$$\frac{\partial A}{\partial t}+\frac{\partial Qc_s}{\partial x}=b\left(E-D\right) \tag{2.12}$$

$$\frac{\partial A_s}{\partial t}=-\frac{b\left(E-D\right)}{1-p} \tag{2.13}$$

where Q is the discharge; A is the cross-sectional flow area, equal to the actual flow area for open channel flow, whereas $A = A_{\max}\,\rho/\rho_0'$ is the equivalent wetted area for pressurized flow, ρ and ρ_0' are the densities of water-sediment mixtures at current pressure and atmospheric pressure; $A_{\max}$ is the full cross-sectional area of the water-sediment mixture in the bottom tunnel; b denotes the flow width; u is the flow velocity; $S_0 = \partial z_b/\partial x$ is the bed slope; A_s is the cross-sectional area of the bed sediment layer. The effective bed shear stress is $\tau_{eff} = \tau_B' + \tau_N'$ where $\tau_B' = \tau_B \chi$ is the shear stress due to non-Newtonian rheology, in which χ is the wetted perimeter, and $\tau_N' = \tau_{fb}' + \tau_{sb}'$ represents boundary resistance for the combined Newtonian fluid and solid phases. I is a pressure term, which depends on the flow regime, according to the Two-component Pressure Approach (TPA) proposed by Vasconcelos and Wright [48], as follows:

$$I = \begin{cases} I'(A) & \text{open-channel flow} \\ I'(A_{\max}) + a^2/g \cdot (A - A_{\max}) & \text{pressurized flow} \end{cases} \tag{2.14}$$

where $I'(A) = 0.5bh^2$ is the hydrostatic pressure force term in open channel flow, and formally appears equivalent to the de Saint-Venant equation, and h is the depth of the water-sediment mixture; $a = \sqrt{gA/T_S}$ is the pressure wave speed, and $T_s = 0.029b$ is the slot width, according to Aureli et al. [49].

A set of relations has to be introduced to close the governing equations. The sediment exchange fluxes (i.e., E and D) are determined following Eqs. (S3, S4) in the Supporting Information. Once the gate of the bottom tunnel is opened, hyper-concentrated flows with significant non-Newtonnian nature frequently occur due to high sediment concentration caused by the collapsed bed. Thus, non-Newtonian rheology is implemented in accordance

with Eqs. (S12a, S12b) in the Supporting Information. Besides, interphase and particle-particle interactions prevail as sediment concentration rises. Therefore the resistances for the Newtonian fluid and solid phases are determined by Manning's equation [40] and the Coulomb friction law [42] respectively as follows :

$$\tau'_{fb} = \rho g \frac{n_b{}^2 Q^2}{A R^{4/3}} \tag{2.15}$$

$$\tau_{sby} = g\chi \cos^2 \varphi' \left(\rho_s - \rho_w\right) Rc_s \tan\phi_{bed} \operatorname{sgn}\left(u\right) \tag{2.16}$$

where n_b is the bed roughness Manning's coefficient, R is the hydraulic radius of the cross section, $\cos\varphi' = 1\Big/\sqrt{1+\left(\partial z_b/\partial x\right)^2}$, and φ' is the angle of the bottom bed of tunnel.

A detailed description of the numerical algorithm is given by Liu et al. [40], where the hyperbolic system is numerically solved using a shock-capturing finite volume method with inter-cell numerical fluxes computed by the HLLC Riemann solver [46].

2.3 Water and sediment exchange between the reservoir and bottom tunnel

Water and sediment exchange between the reservoir module and bottom tunnel module occurs at the tunnel intake, which forms the inner boundary condition and is affected by the flow regime (subcritical flow and supercritical flow), vertically layered flow structures (double layers and single layer), and 2D and 1D computational domains, as shown in Fig.1.

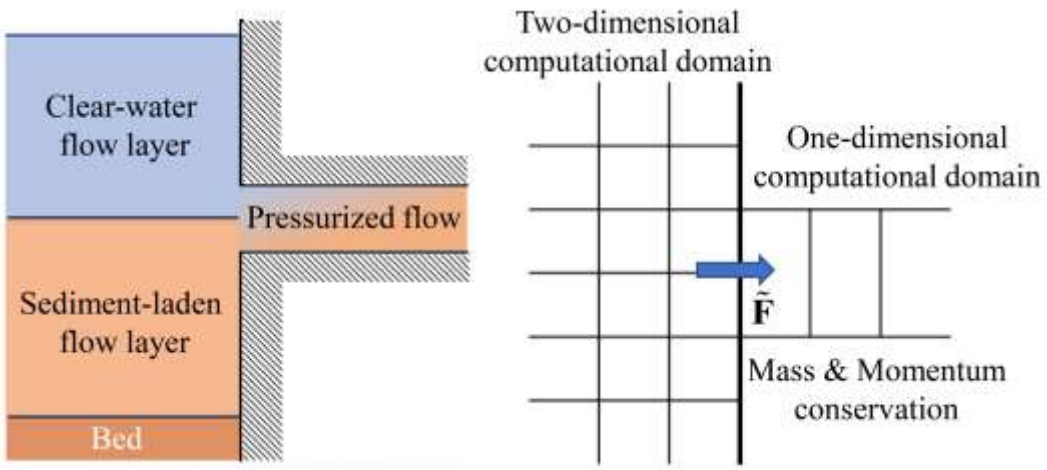

Fig. 1. Interface between reservoir module and bottom tunnel module: (a) side view; and (b) plan view of local computational domain, where $\tilde{\mathbf{F}}$ denotes water and sediment exchange fluxes between the two modules.

A strategy for drainage networks proposed by Liu et al. [50] is adapted to manage the inner boundary condition of the present model. In contrast to the control cell normally used at such a junction in a drainage networks model [50], a ghost cell at the tunnel intake is used in the present coupled model to calculate the water and sediment exchange fluxes according to mass and momentum conservation laws (see Subsection S1.2, Text S1, Supporting Information for details). In brief, a ghost cell is set as the upstream boundary of the bottom tunnel module, with its physical variables (i.e., sediment concentration, flow discharge, and piezometric head) determined from the corresponding variables of several 2D cells near the tunnel intake. The numerical flux at the upstream boundary of the 1D bottom tunnel module is then computed using the HLLC Riemann solver [46, 50]. To ensure mass and momentum conservation between the reservoir and bottom tunnel, the summation of the downstream boundary fluxes of the 2D reservoir module at the tunnel intake must equal the upstream boundary flux of the 1D module. This 1D numerical flux is therefore allocated to the

aforesaid 2D cells as their respective downstream fluxes. Through this procedure, the 2D reservoir module is integrated with the 1D bottom tunnel module with mass and momentum conservation strictly preserved.

3 Computational cases

3.1 Case description

The computational cases simulate a series of physical experiments that were conducted by Xu et al. [25] to investigate threshold conditions for the occurrence of reservoir sediment flushing through a bottom tunnel with an initially covered intake. The experiments were conducted in a glass flume containing a channel (9.0 m long × 1.0 m wide × 0.6 m deep), and an acrylic dam with a bottom tunnel and an overflow weir (0.2 m wide × 0.3 m deep), as shown in Fig. 2. Three kinds of bottom tunnel types were used in the experiments, each with the same square cross-section of height, $h_b = 3.5\,\mathrm{cm}$, and width, $b_b = 3.5\,\mathrm{cm}$. As shown in Figs. 2b1 and 2b2, the bottom tunnel slope of Types A and B was flat ($i_b = 0$), and the tunnel length l_t was 80 cm (Type A) or 40 cm (Type B). The bottom tunnel slope of Type C was steep ($i_b = 0.0067$) with a curved section, as shown in Fig. 2b3.

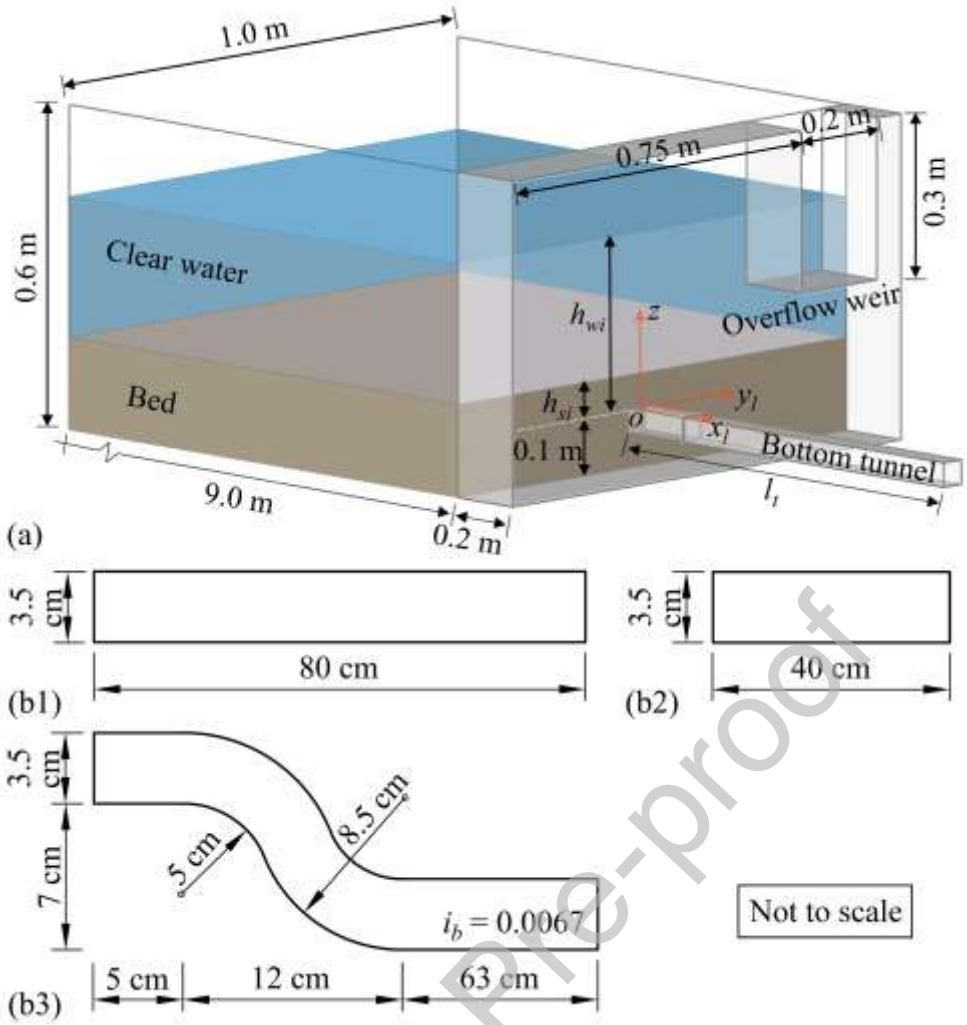

Fig. 2. (a) Schematic diagram of flume geometry containing a dam, bottom tunnel, and outflow weir; (b1-b3) Profile views of three types of bottom tunnels. (Adapted from Xu et al. [25], reproduced with permission)

In the experiments of Xu et al. [25], a grid was set at the flume inlet, and a flat gate was installed at the tunnel intake. A constant-head tank and a butterfly valve were used to regulate the clear water inflow. The water level downstream of the dam was kept below the outlet of the bottom tunnel, and the fluid flowing out of the tunnel entered the air. In the pre-experiments, the gate of the overflow weir was closed and the gate of the bottom tunnel was fully open, until the clear-water flow became steady in accordance with the controlled reservoir water level; the inflow discharge Q_i was then measured. At the start of each case,

the gate of the bottom tunnel was opened quickly, and the weir gate was adjusted to keep the reservoir water level h_{wi} constant.

Natural fine sand was used to represent non-cohesive sediment deposits in a reservoir. According to the published data, the sediment was nearly uniform with median diameter $d_{50} = 0.147$ mm and density $\rho_s = 2650\,\mathrm{kg/m^3}$. The porosity of the sediment deposits was $p = 0.428$.

3.2 Modelling conditions and parameters

Table 1 summarizes the six experimental cases [25] selected for the simulations, based on combinations of different conditions, i.e., the cover layer thickness h_{si}, the reservoir water level h_{wi}, the tunnel length l_t, and the tunnel slope i_b. By considering different combinations of conditions, it is possible to examine distinct water-sediment behaviour encountered in reservoir sediment flushing, i.e., SF (sediment flushing) and TB (tunnel blockage). SF means that sediment in the reservoir is scoured and transported downstream through the tunnel, and the outflow is almost clear water when SF is accomplished. By contrast, TB means that sediment near the intake is entirely deposited in the tunnel.

Table 1. Parameter values for simulations corresponding to experiments [25].

Numerical case	h_{si} (m)	h_{wi} (m)	Q_i (L/s)	Bottom tunnel type	Experimental case (outcome) [25]
A	0.130	0.414	3.030	Type A	A22 (SF)
B1	0.130	0.368	2.840		A21 (SF)
B2	0.130	0.264	2.430		A16 (TB)

C1	0.146	0.414	3.030		A30 (SF)
C2	0.190	0.414	3.030		A44 (TB)
D1	0.130	0.264	2.680	Type B	B48 (SF)
D2	0.130	0.264	2.570	Type C	C57 (SF)

Fig. 2 shows the 2 m long reach with an initially horizontal sediment bed upstream of the dam and the dam with the overflow weir and the bottom tunnel which were modelled in the simulations. A fixed-bed, steady flow simulation is first considered, with the resulting flow hydrodynamics taken as the initial condition, with gradually varied clear-water inflow of discharge Q_i specified at the inlet and constant reservoir water level h_{wi} imposed immediately upstream of the dam (Table 1). At the reservoir inlet cross section, the prescribed discharge Q_i determines the boundary conditions for the clear-water flow layer in the absence of a sediment-laden flow layer. The upstream boundary condition is implemented using the method of characteristics. A free outflow boundary is applied at the outlet cross section of the bottom tunnel, and a flux computation approach is adopted to keep the clear-water flow layer at constant water level h_{wi} at the overflow weir. Solid wall boundary conditions for the upper clear-water flow layer and the lower sediment-laden flow layer at the dam wall are implemented using the flux computation approach suggested by Hou et al. [51].

The same fixed uniform meshes are adopted in all cases, with mesh independence ensured as shown in Fig. S2 of the Supporting Information. The converged spatial step is 0.005 m in both longitudinal and lateral directions in the 2D model and in the longitudinal direction of the 1D model. The interface roughness Manning's coefficient in the reservoir

module is set to $0.005\,\mathrm{m}^{-1/3}\mathrm{s}$, following Cao et al. [29]. The Courant number is set to 0.4. Table 2 lists the values of the Coulomb friction coefficient $\tan\phi_{bed}$, the bed roughness Manning's coefficient n_b, and the saturation recovery coefficient α used for model closure. These parameters are calibrated based on Case C1, with the obtained values adopted in all the other cases.

Table 2. Summary of model parameter values and typical ranges.

Parameter	Meaning (units)	Range	Value
$\tan\phi_{bed}$	Coulomb friction coefficient	$[0,1]$	0.3
n_b	Bed roughness Manning's coefficient ($\mathrm{m}^{-1/3}\mathrm{s}$)	$[0.01,0.02]$	0.015
α	Saturation recovery coefficient	$[0.5,2]$	1.2

4 Results and discussion

4.1 General description

The intake of the bottom tunnel is initially covered by sediment deposits. Once the tunnel gate is opened, the bed material collapses quickly due to the bed slope being larger than the repose angle, and the collapsed sediment enters the ambient clear-water flow, producing a double-layer flow structure composed of a subaqueous highly concentrated sediment-laden flow layer (i.e., turbidity current) immediately above the bed and an upper clear-water flow layer. Sediment deposits upstream of the dam are scoured and transported downstream through the tunnel, and eventually, the outflow comprises almost clear water, at which point sediment flushing has been accomplished (SF), as shown in Figs. 3a1 and 3a2. Otherwise, if the hyper-concentrated sediment-laden flow is hindered by boundary resistance, and

eventually the tunnel becomes completely blocked by sediment deposits, then tunnel blockage has occurred (TB), as shown in Figs. 3b1 and 3b2.

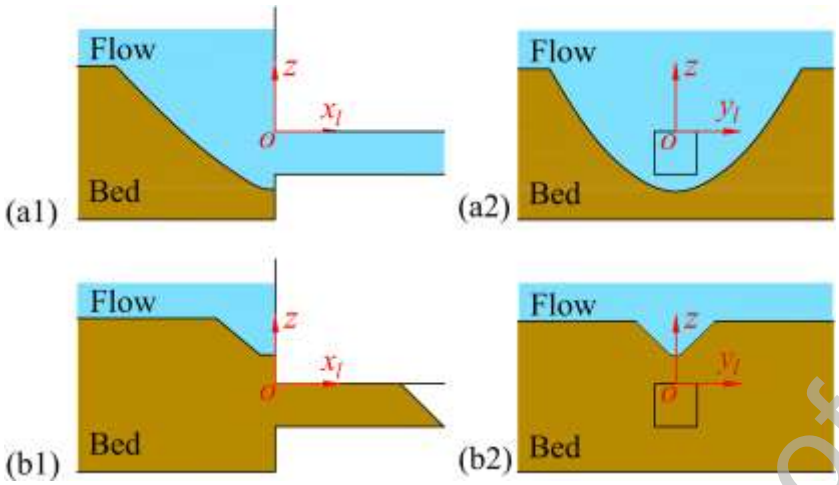

Fig. 3. Schematic diagram of topography near the tunnel intake: (a1-a2) SF geometry in profile view and cross-sectional view; (b1-b2) TB geometry in profile view and cross-sectional view.

4.2 Hydro-sediment-morphodynamic process of flushing

Two conventional metrics are introduced for quantitative evaluation, i.e., the percentage bias (PBIAS) [52], and the coefficient of determination (R^2):

$$\mathrm{PBIAS} = \frac{\sum_{i=1}^{n}\left(E_i^{\mathrm{obs}} - E_i^{\mathrm{com}}\right)}{\sum_{i=1}^{n}\left(E_i^{\mathrm{obs}}\right)} \tag{4.1}$$

$$\mathrm{R}^2 = \frac{\left(\sum_{i=1}^{n}\left(E_i^{\mathrm{obs}} - \bar{E}^{\mathrm{obs}}\right)\left(E_i^{\mathrm{com}} - \bar{E}^{\mathrm{com}}\right)\right)^2}{\sum_{i=1}^{n}\left(E_i^{\mathrm{obs}} - \bar{E}^{\mathrm{obs}}\right)^2 \sum_{i=1}^{n}\left(E_i^{\mathrm{com}} - \bar{E}^{\mathrm{com}}\right)^2} \tag{4.2}$$

where E_i^{obs} represents observed data i; $\bar{E}^{\mathrm{obs}}$ is the mean value of the observed values; E_i^{com} represents computed data i; $\bar{E}^{\mathrm{com}}$ is the mean value of the computed values; and n is the number of the observations. PBIAS illustrates the tendency of the numerical prediction to be larger or smaller than its measured counterpart, and a value of zero means

the fit is good. The closer R^2 is to 1, the smaller the discrepancy.

Model calibration is conducted by comparing the computational results with published experimental data [25] on bed elevation profiles at different cross sections. Cases C1 and A are considered herein for model calibration and validation, because accurate cross-sectional topographic data near the tunnel intake of other cases were not measured in experiments. For Case C1 (see Fig. S3, Supporting Information), the corresponding computed results for bed elevation agree satisfactorily with measured data, as confirmed by the percentage bias ($|\text{PBIAS}| \le 0.20$) and correlation coefficient ($R^2 \ge 0.92$) values.

Using coefficients calibrated from Case C1 (i.e., $\tan\phi_{bed} = 0.3$, $\alpha = 1.2$, and $n_b = 0.015\,\text{m}^{-1/3}\text{s}$), the numerically predicted values of bed elevation at different cross sections for Case A also agree well with the measured data, as shown in Fig. 4 and confirmed by the percentage bias ($|\text{PBIAS}| \le 0.28$) and correlation coefficient ($R^2 \ge 0.97$) values. At $t = 30\,\text{s}$, with sediment flushing taking place, the bed surface forms a funnel-shaped scour hole upstream of the intake. At each cross section, the bed profile z_b is parabolic with a low centre and high sides. The closer to the intake along the central axis ($y_l = 0\,\text{m}$), the lower the bed elevation. At $t = 60\,\text{s}$, the scour hole has further deepened and widened. By $t = 180\,\text{s}$, sediment upstream of the intake has been transported and deposited at the bottom of the scour hole, after which further bed deformation is negligible, and the shape of the scour hole is stable.

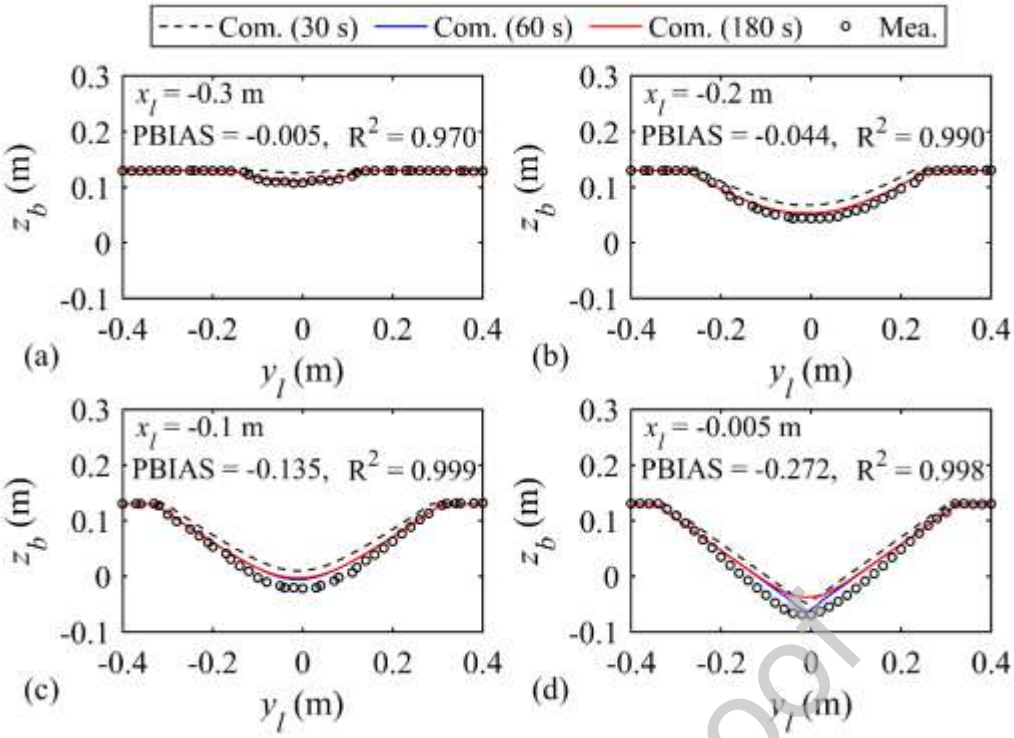

Fig. 4. Case A, computed and measured [25] bed elevation profiles at different cross sections: (a) $x_l = -0.3\,\mathrm{m}$, (b) $x_l = -0.2\,\mathrm{m}$, (c) $x_l = -0.1\,\mathrm{m}$, and (d) $x_l = -0.005\,\mathrm{m}$.

Here we evaluate the hydro-sediment-morphodynamic process of reservoir sediment flushing based on the numerical simulation of Case A. Fig. 5 shows computed water surface elevation η_w, interface elevation η_s, piezometric head and bed elevation z_b profiles along the central axis ($y_l = 0\,\mathrm{m}$) of the reservoir and the bottom tunnel for Case A at different times, as well as measured data and empirical formulations [25] for the equilibrium scour-hole geometry. At initial time $t = 0\,\mathrm{s}$, the flat gate at the tunnel intake is closed, and sediment deposits upstream of the dam remain static. Only the clear-water flow layer and bed layer exist in the reservoir. By $t = 1\,\mathrm{s}$, the tunnel gate has been opened, and collapsed sediments have entered the ambient flow, producing a double-layer flow structure composed of an upper clear-water flow layer and a subaqueous sediment-laden flow layer (i.e., turbidity current). As the turbidity current propagates downstream along the bottom tunnel,

the interface between the clear-water layer and sediment-laden layer forms a funnel-shaped morphology upstream of the intake, and the sediment-laden flow turns, becoming pressurized with an inclined front in the bottom tunnel. At $t = 30\,\mathrm{s}$, bed-layer sediment is scoured and transported into the tunnel. The sediment-laden flow layer thickness has reduced upstream of the tunnel intake, while the water-sediment mixture under the larger piezometric head fills the bottom tunnel. At $t = 60\,\mathrm{s}$, the interface between the two layers lies below the upper edge of the tunnel intake, and both the sediment-laden and clear-water flow layers enter the tunnel. The bed is continuously eroded, and the scour hole deepens. At $t = 180\,\mathrm{s}$, the funnel-shaped scour hole exhibits slight aggradation below the tunnel intake because of sediment deposition, and only a single layer clear-water flow structure exists in the reservoir and bottom tunnel. Besides, the bed elevation near the tunnel intake at $t = 180\,\mathrm{s}$ is higher than that at $t = 60\,\mathrm{s}$. This is because constant deposition occurs near the bottom tunnel intake due to basically zero velocity, as the vertical velocity cannot be resolved in the present model.

Compared with the measured data and the empirical formulations of Xu et al. [25], the computed bed elevation at the upstream edge of the funnel-shaped scour hole is approximately the same, while that near the tunnel intake is slightly higher than Xu et al.'s at $t = 180\,\mathrm{s}$. This is mainly because the present 2D model cannot reflect the aspiration mechanism for turbidity current outflow from tunnel intake [3], which is mainly controlled by the vertical velocity components. Thus, when the computed interface elevation η_s is below the floor level of the tunnel intake, sediment upstream of the intake deposits at the bottom of scour hole without outflow of the sediment-laden flow layer.

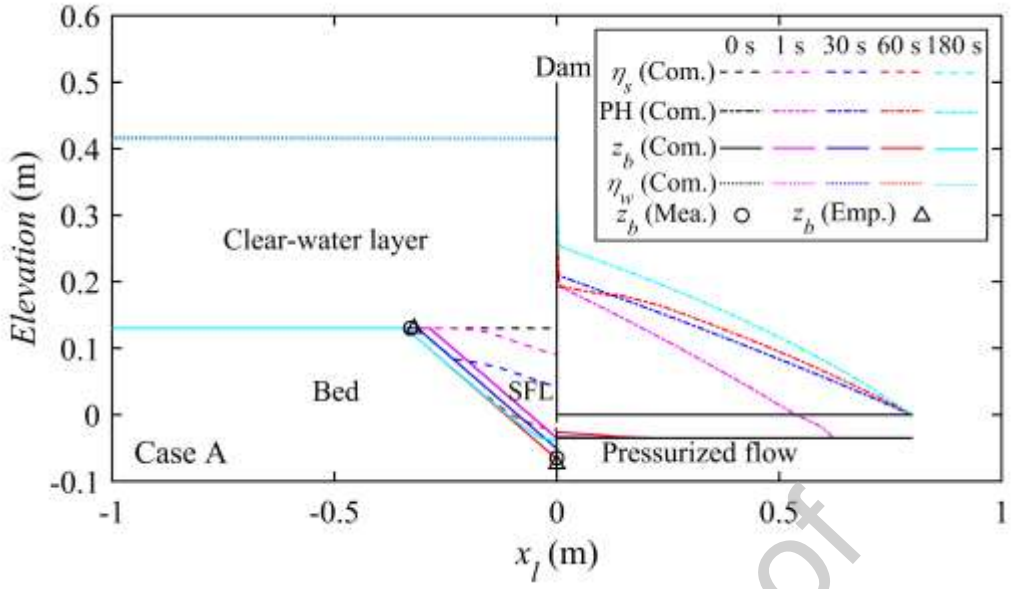

Fig. 5. Case A, computed water surface η_w, interface η_s, piezometric head (PH), and bed elevation z_b profiles along the central axis $y_l = 0\,\mathrm{m}$ at different times, as well as bed elevations from observation and empirical formulations of Xu et al. [25], where SFL denotes sediment-laden flow layer.

Fig. 6 presents four snapshots in time of the interface elevation η_s and bed morphology z_b for Case A. By $t = 1\,\mathrm{s}$, sediment in collapsing areas where the local bed slope exceeds the repose angle has entered the ambient flow and formed a lower sediment-laden flow layer of high concentration (Fig. 6a). As the sediment is transported through the bottom tunnel, the interface between the sediment-laden flow layer and clear-water flow layer takes the form of a shallow funnel upstream of the tunnel intake, which is symmetrical about the central axis ($y_l = 0\,\mathrm{m}$). By $t = 30\,\mathrm{s}$, the bed has been continuously eroded, causing the scour hole to widen. The elevation of interface η_s is lower than before, and water-sediment mixtures entirely fill the bottom tunnel (Fig. 6b). At $t = 60\,\mathrm{s}$, the scour hole has continued to grow both in depth and width, the interface

elevation η_s is below the upper edge of the tunnel intake, and both flow layers enter the tunnel (Fig. 6c). Finally, by $t = 180\,\mathrm{s}$, the sediment-laden flow layer has disappeared because of sediment deposition on the bed, and the bed exhibits slight aggradation below the tunnel intake (Fig. 6d).

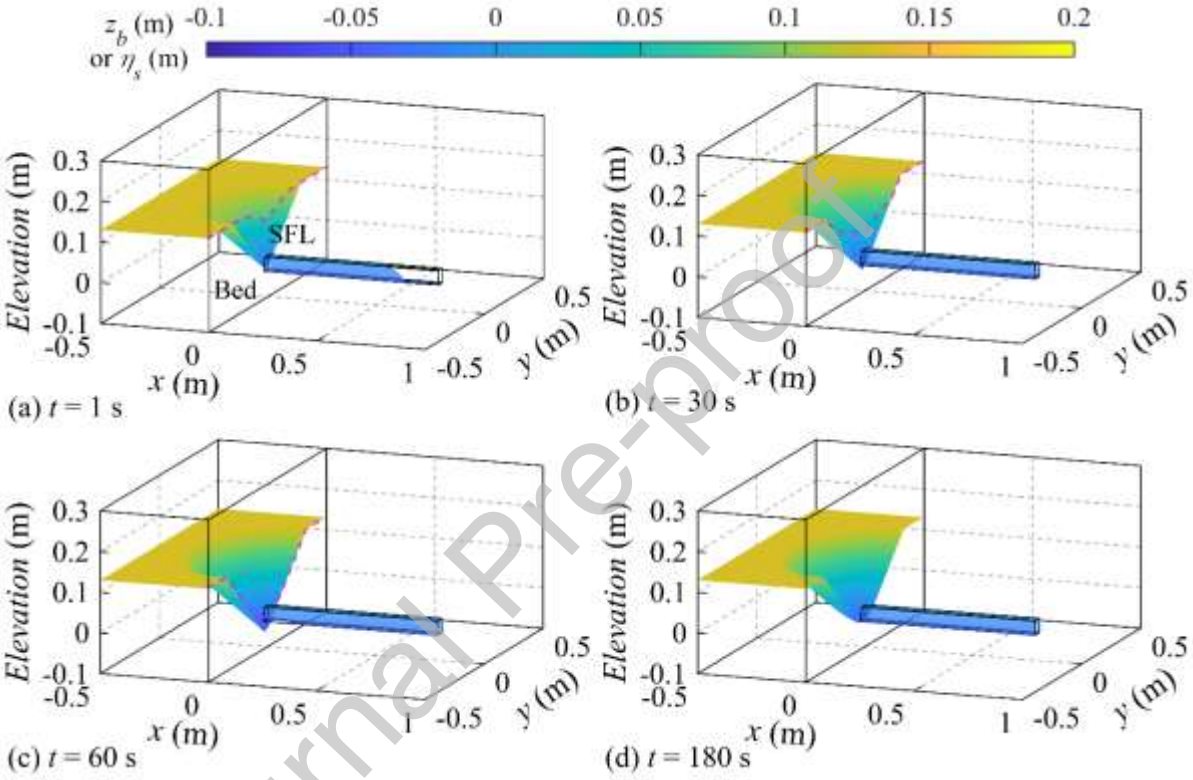

Fig. 6. Case A, three-dimensional view of the upper surface of the sediment-laden flow layer η_s and bed z_b at times: (a) $t = 1\,\mathrm{s}$; (b) $t = 30\,\mathrm{s}$; (c) $t = 60\,\mathrm{s}$; and (d) $t = 180\,\mathrm{s}$.

Fig. 7 shows the velocity fields of the clear-water flow layer U_{mw} and the sediment-laden flow layer U_{ms} near the tunnel intake. At $t = 1\,\mathrm{s}$, the interface elevation η_s between the two layers is higher than the upper edge of tunnel intake (Fig. 5), and only clear water flows through the overflow weir (Fig. 7a1) while the highly concentrated sediment-laden flow layer enters the bottom tunnel (Fig. 7a2). At $t = 60\,\mathrm{s}$, the interface elevation η_s is lower than the upper edge of tunnel intake (Fig. 5), and flows from both

layers enter the tunnel (Figs. 7b1 and 7b2). The velocity of sediment-laden flow layer upstream of the intake is larger as the layer thickness is smaller, and the velocity of the low concentration, sediment-laden flow in the tunnel is larger than earlier at $t = 1\,\mathrm{s}$ (Figs. 7a2 and 7b2).

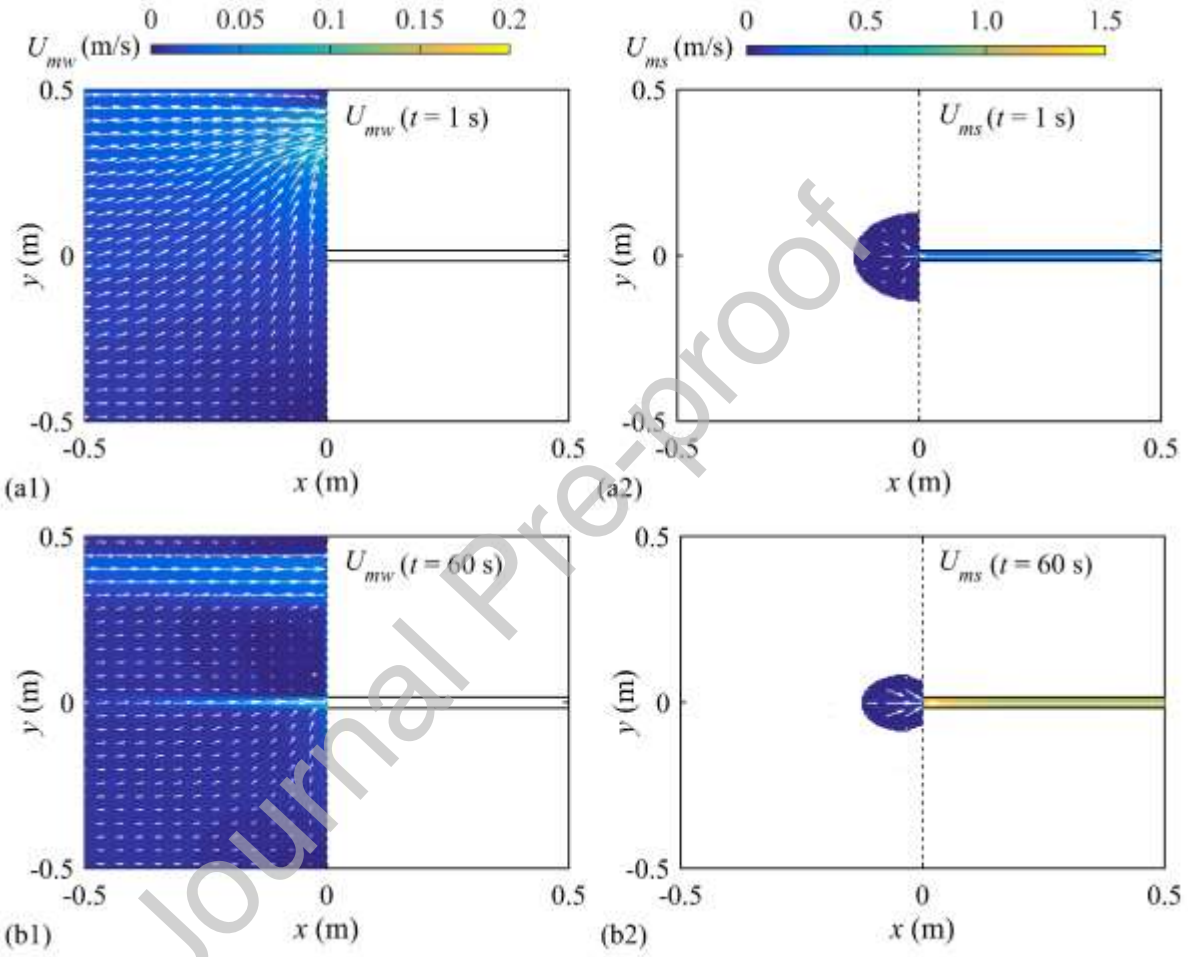

Fig. 7. Case A, plan view velocity fields of (1) the clear-water flow layer U_{mw}, and (2) the sediment-laden flow layer U_{ms} at (a) $t = 1\,\mathrm{s}$ and (b) $t = 60\,\mathrm{s}$.

Figs. 8, 9 and 10 illustrate the volumetric sediment concentration c_s and longitudinal and transverse sediment transport rates per unit width in the vicinity of the tunnel intake. As the tunnel intake gate is opened, a turbidity flow with high sediment concentration vents through the intake. The sediment concentration in the reservoir and tunnel generally decreases with time until the outflow is composed of almost clear water (Fig. 8) and the

longitudinal sediment transport rate per unit width remains below 60 cm^2/s (Fig. 9). From t = 1 s to 30 s, the volumetric sediment concentration c_s of sediment-laden flow in both the reservoir and tunnel is fairly high because of collapsed sediment from the bed layer entering the ambient fluid (Figs. 8a and 8b). The velocity of sediment-laden flow in the tunnel is much higher than that in the reservoir (Fig. 7a2), and so drives a larger rate of longitudinal sediment transport in the tunnel (Figs. 9a and 9b). Besides, the closer the sediment-laden flow is to the intake, the larger its transverse velocity and transverse sediment transport rate (Figs. 10a and 10b). From t = 30 s to 60 s, the sediment concentration and sediment transport rate of the sediment-laden flow in the tunnel gradually decrease after mixing with clear water and venting through the outlet (Figs. 8c, 9c and 10c). Finally, at $t = 180\,\mathrm{s}$, only the clear-water flow layer enters the tunnel, and the sediment concentration and sediment transport rate decrease to zero (Figs. 8d, 9d and 10d).

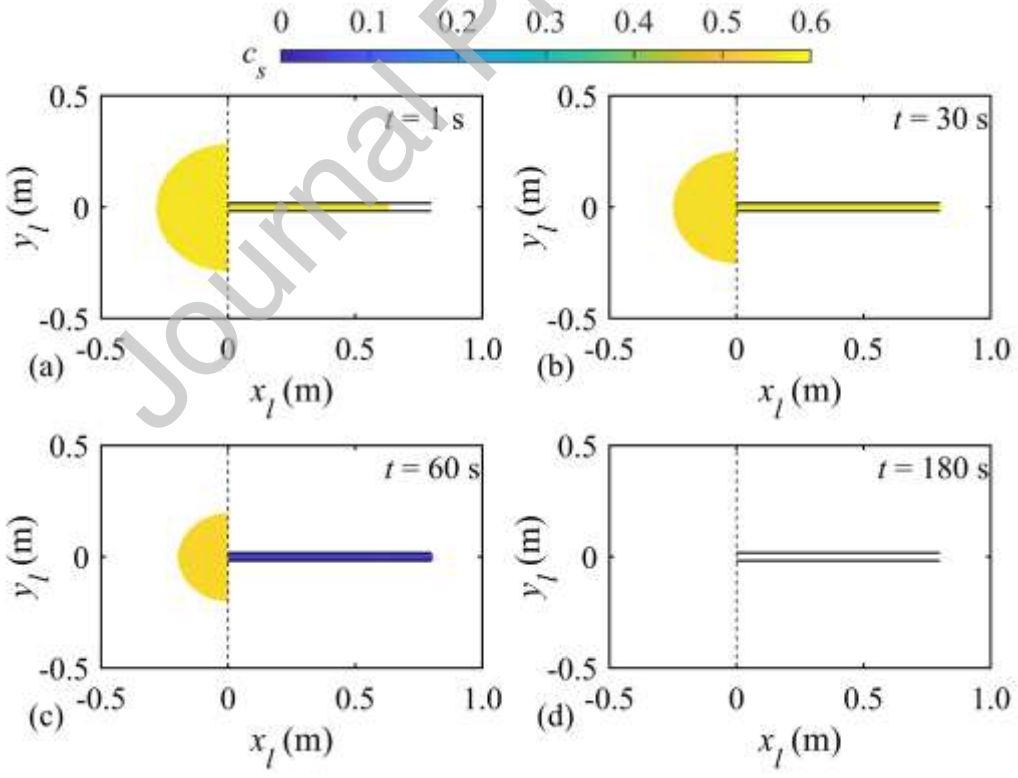

Fig. 8. Case A, plan views of the distribution of volumetric sediment concentration c_s of the sediment-laden flow layer at times: (a) $t = 1\,\mathrm{s}$; (b) $t = 30\,\mathrm{s}$; (c) $t = 60\,\mathrm{s}$ and (d)

$t = 180\,\mathrm{s}$.

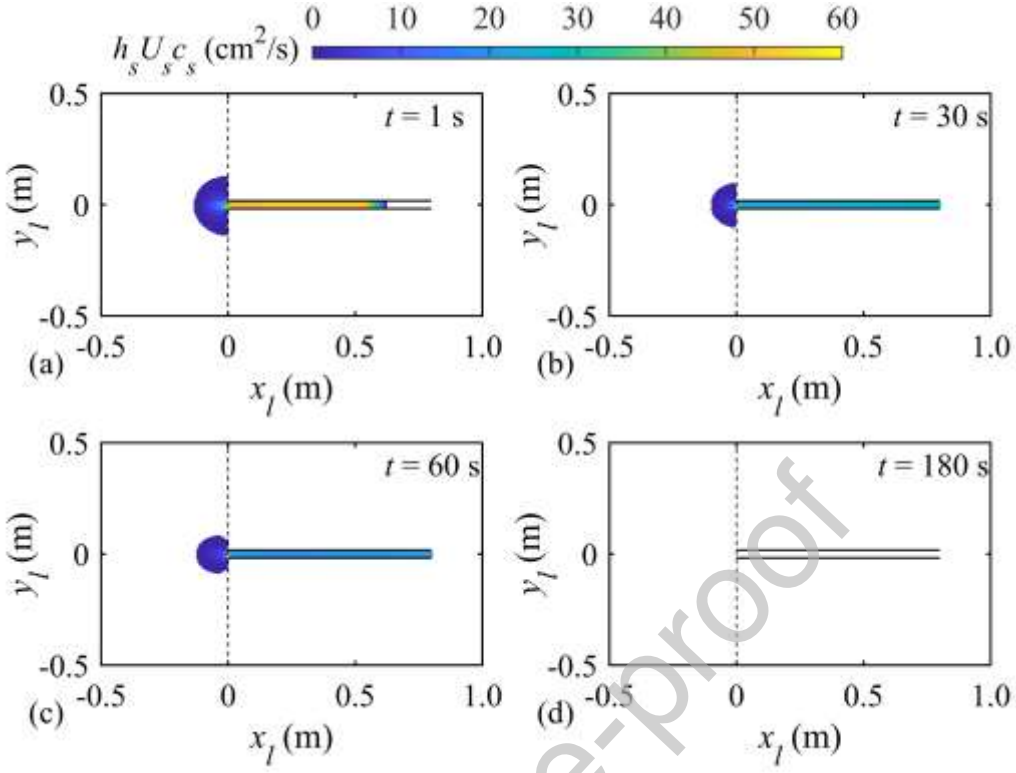

Fig. 9. Case A, plan views of the distribution of longitudinal sediment transport rate per unit width $h_s U_s c_s$ of the sediment-laden flow layer at times: (a) $t = 1\,\mathrm{s}$; (b) $t = 30\,\mathrm{s}$; (c) $t = 60\,\mathrm{s}$ and (d) $t = 180\,\mathrm{s}$.

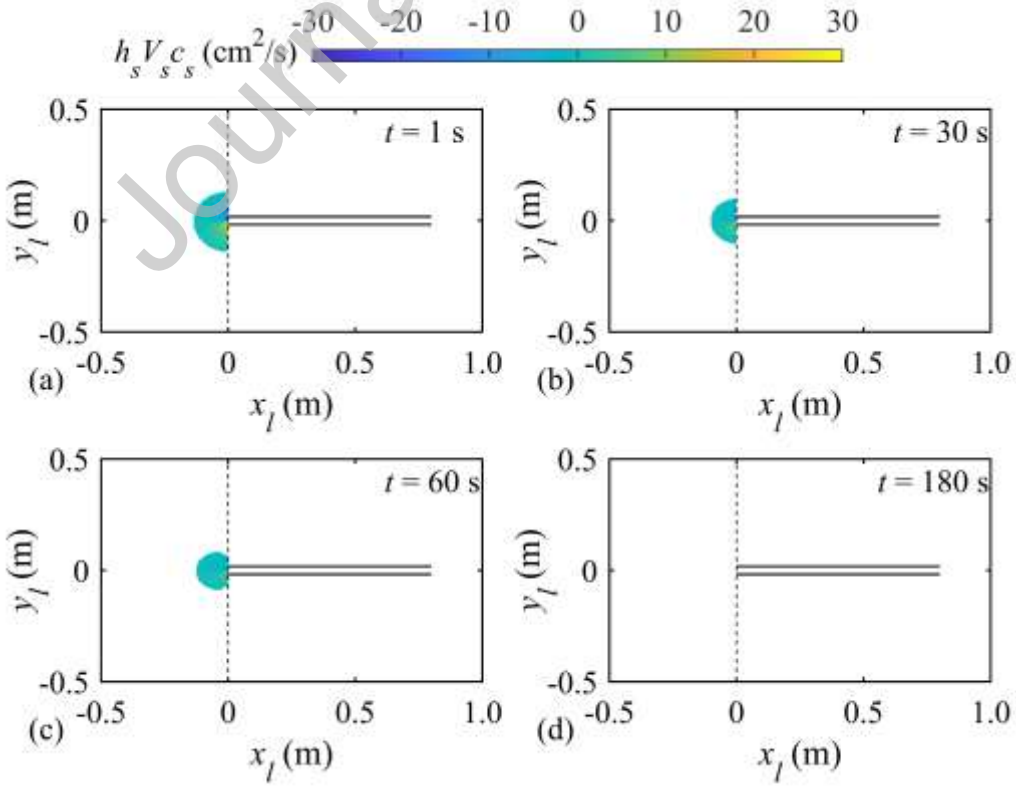

Fig. 10. Case A, plan views of the transverse sediment transport rate per unit width $h_s V_s c_s$ of the sediment-laden flow layer at times: (a) $t = 1\,\mathrm{s}$; (b) $t = 30\,\mathrm{s}$; (c) $t = 60\,\mathrm{s}$ and (d) $t = 180\,\mathrm{s}$.

Fig. 11 displays the bed shear stress τ_{eff} of the sediment-laden flow layer for Case A at four cross sections in the reservoir and the bottom tunnel. The bed shear stress τ_{eff} is related to the sediment concentration, velocity, and thickness of the sediment-laden flow layer, and the contact area between the flow and boundary. In general, for cases where sediment flushing is ultimately accomplished, the bed shear stress τ_{eff} of the sediment-laden flow layer gradually decreases over time with diminishing sediment concentration and thickness at any given cross section in both the reservoir and tunnel. Meanwhile, the closer the sediment-laden flow layer is to the tunnel intake, the larger is the bed shear stress τ_{eff} in the reservoir (Figs. 11a1 and 11a2) and the smaller is the bed shear stress τ_{eff} in the bottom tunnel (Figs. 11b1 and 11b2).

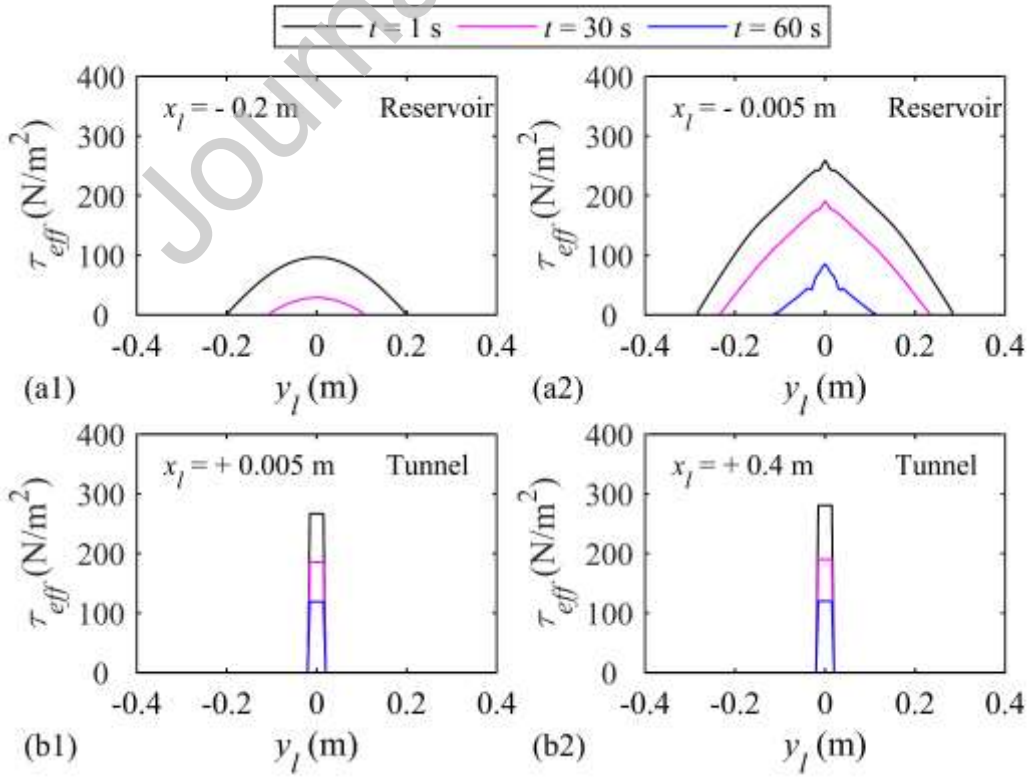

Fig. 11. Case A, bed shear stress τ_{eff} of sediment-laden flow layer at times t = 1, 30 and 60 s at two cross sections upstream of the intake, (a1) $x_l = -0.2\,\mathrm{m}$ and (a2) $x_l = -0.005\,\mathrm{m}$, and two cross sections in the bottom tunnel, (b1) $x_l = +0.005\,\mathrm{m}$ and (b2) $x_l = +0.4\,\mathrm{m}$.

4.3 Flushing versus blocking

The occurrence of SF or TB is primarily controlled by reservoir water level, cover layer thickness, and tunnel type (i.e., length and slope), as is further demonstrated in the following subsections.

4.3.1 Effect of reservoir water level

By considering the computed results for Cases B1 and B2, we now probe into the effect of reservoir water level h_{wi} on sediment flushing. Fig. 12 displays the computed water surface elevation η_w, interface elevation η_s, piezometric head and bed elevation z_b profiles along the central axis ($y_l = 0\,\mathrm{m}$) of the equilibrium scour hole geometry for Cases B1 and B2 at different times, along with measured data and the empirical formulations [25]. As shown in Figs. 12a and 12b, the reservoir water level of Case B1 is higher than that of Case B2. Fig. 13 shows the time histories of the computed interface elevation η_s and bed morphology z_b for Case B2. As can be seen in Figs. 12a and 12b, at t = 1 s, both Case B1 and Case B2 present a double layer flow structure composed of an upper clear-water flow layer and a lower sediment-laden flow layer. In Case B1, with a higher water level, a deeper funnel-shaped morphology formed by the interface between two layers develops in the reservoir, and the front tends to advance more quickly in the tunnel. By $t = 15\,\mathrm{s}$, the results for Case B1 have diverged from those for Case B2 owing to the difference in reservoir water

level. In Case B1, the higher water level induces a larger piezometric head behind the intake in the tunnel without bed aggradation. By contrast, in Case B2, sediment from the turbidity current layer is deposited upstream of the intake and inside the tunnel (Fig. 12b). The lowest point of the funnel-shaped bed morphology is located close to the upper edge of the tunnel intake, and the thickness of the deposited layer in the tunnel has increased but is still below the roof of the tunnel (Fig. 13b). At $t = 30\,\mathrm{s}$, in Case B1, the deepening process of the scour hole slows down upstream of the tunnel intake, with the lowest point of the scour hole lying below the intake invert. Meanwhile, in Case B2, the thickness of the deposited layer has gradually increased over time; the downstream end of the deposit maintains a gentle slope, and the lowest point of the scour hole is much higher than the roof of the intake in the reservoir (Figs. 12b and 13c). Finally, at $t = 180\,\mathrm{s}$, in Case B1, a single clear-water flow layer exists in the reservoir and bottom tunnel, and the funnel-shaped scour hole is stable, indicating that sediment flushing has been accomplished (Fig. 12a). But in Case B2, the tunnel intake is covered by deposited sediment, and the thickness of the deposited layer in the tunnel is the same as the height of the bottom tunnel, indicating that the tunnel is entirely blocked (Figs. 12b and 13d). This occurs primarily because the pressure difference between the intake and outlet of the tunnel is smaller for the lower reservoir water level, so much so that the driving force is insufficient to overcome the boundary resistance.

Compared with the measured data and the empirical formulations of Xu et al. [25], the computed bed elevation for Case B1 (SF) is slightly different at $t = 180\,\mathrm{s}$ (Fig. 13a) and that for Case B2 (TB) is different at $t = 180\,\mathrm{s}$ (Fig. 13b). For Case B2, when the tunnel is completely blocked by sediment deposits, experimental results show that small amounts of

water may seep out and take away particles through the entirely blocked intake due to pore water pressure [25]. By contrast, when neglecting pore water pressure in the present model, the computed results indicate that the total sediment upstream of the intake deposits at the scour hole and flattens its bottom. Overall, the present model successfully reflects the occurrence of SF and TB under different conditions of reservoir water level, and the computed scour hole geometries agree well with the measured data for the case involving SF.

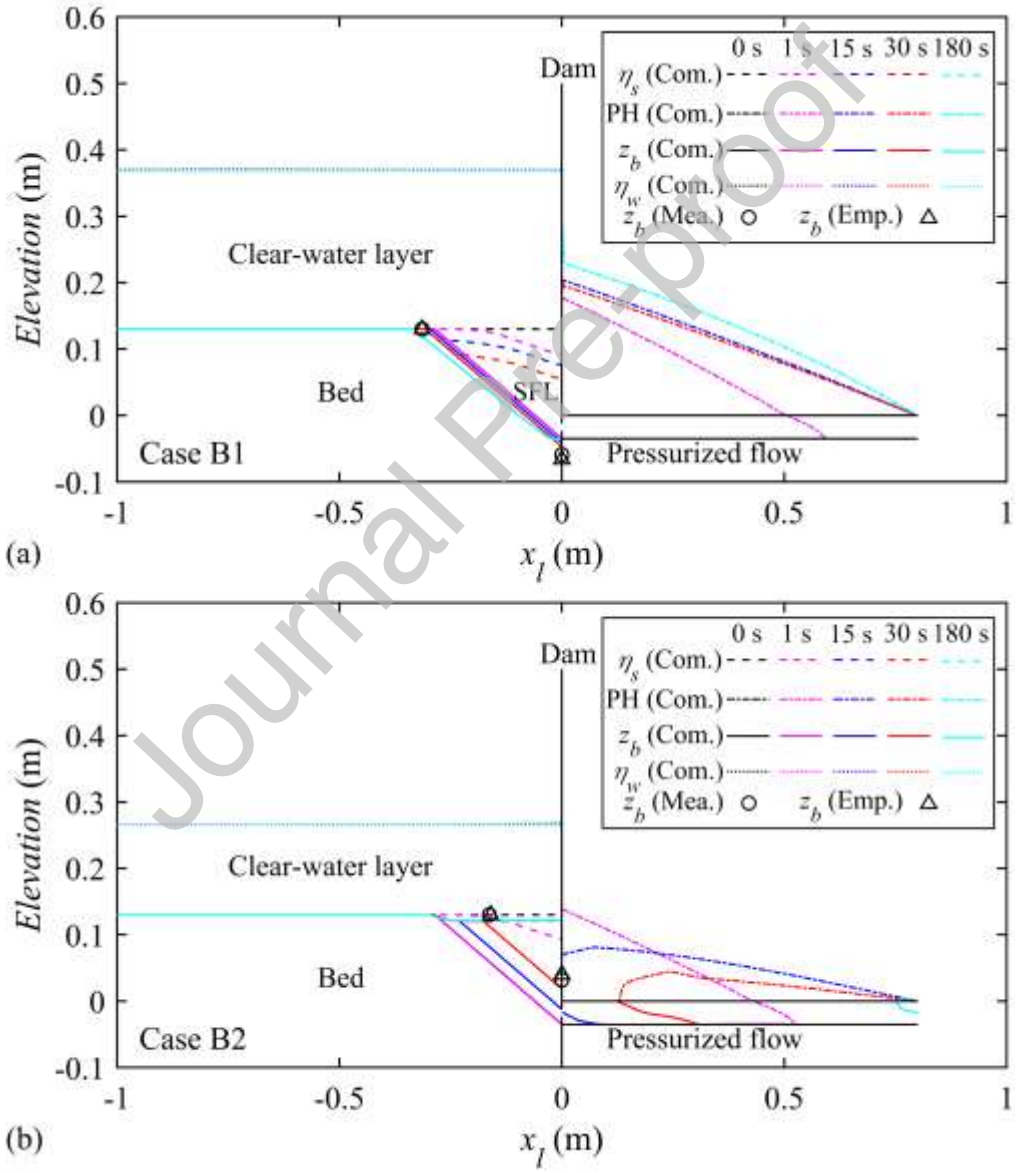

Fig. 12. (a) Case B1 and (b) Case B2, computed water surface η_w, interface η_s, piezometric head (PH), and bed elevation z_b profiles along the central axis $y_l = 0\,\mathrm{m}$ at different times,

as well as bed elevation from observation and the empirical formulations of Xu et al. [25], where SFL denotes sediment-laden flow layer.

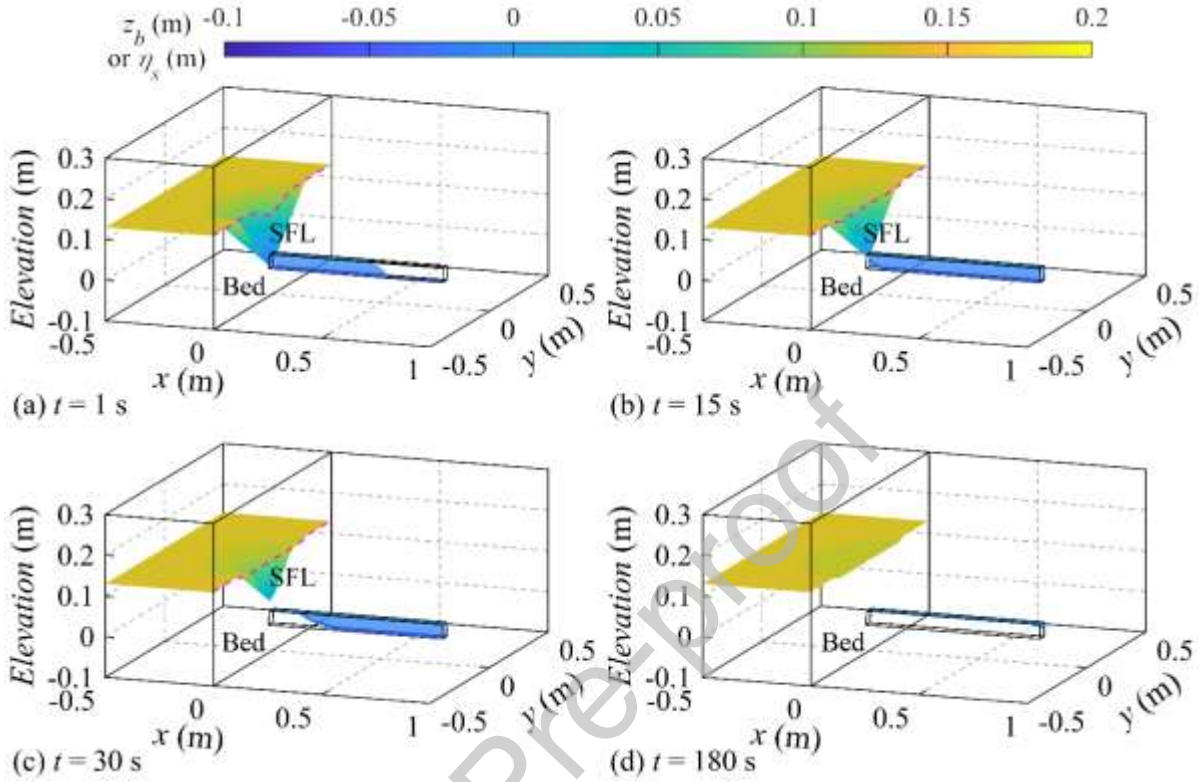

Fig. 13. Case B2, three-dimensional view of the upper surface of sediment-laden flow layer η_s and bed z_b at times: (a) $t = 1\text{s}$; (b) $t = 15\text{s}$; (c) $t = 30\text{s}$; and (d) $t = 180\text{s}$.

Fig. 14 shows the bed shear stress τ_{eff} of the sediment-laden flow layer for Cases B1 and B2 at four cross sections in the reservoir and tunnel. In Case B2, at $x_l = -0.2\,\text{m}$, the bed shear stress decreases from approximately $100\,\text{N/m}^2$ to zero as the turbidity current recedes (Fig. 14a1). At $x_l = -0.005\,\text{m}$, from $t = 1\,\text{s}$ to 15 s, the bed shear stress initially increases, mainly because of the larger flow velocity field near the partially blocked intake. Then, at $t = 30\,\text{s}$, as the intake becomes completely blocked by sediment deposits, the bed shear stress decreases due to the smaller flow velocity and thickness of the turbidity current (Fig. 14a2). At $x_l = +0.005\,\text{m}$ and 0.4 m, as the thickness of the deposition layer

approaches the tunnel height, the bed shear stress in the tunnel gradually decreases to zero (Figs. 14b1 and 14b2). At $t = 15\,\mathrm{s}$, although the bed resistance in Case B2 at other sections is smaller than that in Case B1, at the cross section $x_l = -0.005\,\mathrm{m}$, the bed resistance in Case B2 is larger, promoting sediment deposition and bed aggradation near the intake. Notably, in contrast to Case B2, the higher water level in Case B1 leads to a larger pressure difference between the intake and outlet of the tunnel, which suffices to drive the water-sediment mixture downstream through the outlet, overcoming resistance from the tunnel boundary. Thus, a high reservoir water level favors the occurrence of reservoir sediment flushing.

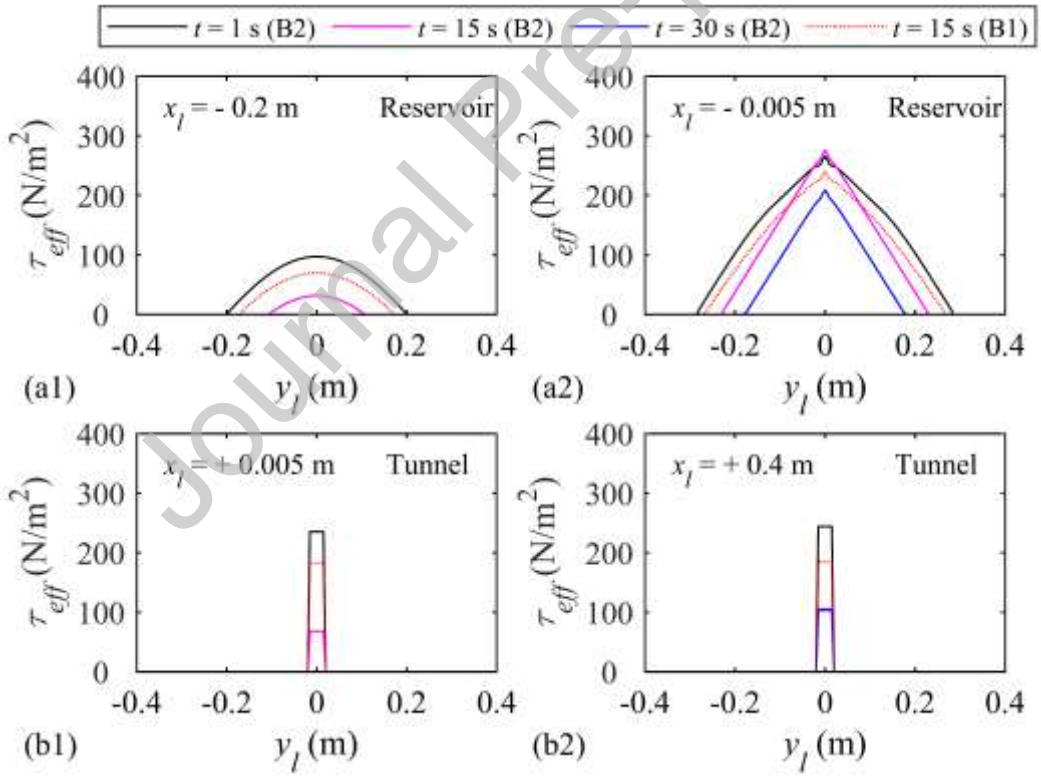

Fig. 14. Cases B1 and B2, bed shear stress τ_{eff} of the sediment-laden flow layer at different times at two cross sections upstream of the intake, (a1) $x_l = -0.2\,\mathrm{m}$, and (a2) $x_l = -0.005\,\mathrm{m}$, and two cross sections in the bottom tunnel, (b1) $x_l = +0.005\,\mathrm{m}$, and (b2) $x_l = +0.4\,\mathrm{m}$.

4.3.2 Effect of cover layer thickness above tunnel intake

We next investigate the effect of cover layer thickness h_{si} on sediment flushing by comparing the simulations for Cases C1 and C2. Fig. 15 shows the computed water surface elevation η_w, interface elevation η_s, piezometric head, and bed elevation z_b profiles along the central axis ($y_l = 0\,\mathrm{m}$) for Cases C1 and C2 at different times. Also depicted are measured data and empirical formulations [25] for the equilibrium scour hole geometry. As shown in Figs. 15a and 15b, the cover layer thickness of Case C1 is smaller than that of Case C2. Fig. 16 displays the temporal development of the interface elevation η_s and bed morphology z_b for Case C2.

Figs. 15a and 15b show that a double layer flow structure composed of an upper clear-water flow layer and a lower sediment-laden flow layer exists at $t = 1\,\mathrm{s}$ in both Cases C1 and C2. For the higher cover layer thickness in Case C2, a larger piezometric head is induced behind the intake, causing the flow front to travel faster along the tunnel. At $t = 30\,\mathrm{s}$, a further deepening of the funnel-shaped interface morphology occurs upstream of the intake in Case C1, and the deposit layer thickness inside the tunnel is smaller than in Case C2 (Fig. 15a). At $t = 60\,\mathrm{s}$, in Case C2, the rate of decrease in turbidity current thickness slows, with the lowest point of the interface being located significantly above the upper edge of the intake (Figs. 15b and 16c). By contrast, the lowest point of the interface in Case C1 is near the roof of the intake, and a large amount of sediment is flushed through the tunnel where the thickness of the deposited layer has reduced (Fig. 15a). Finally, by $t = 180\,\mathrm{s}$, in Case C2, the hyper-concentrated sediment-laden flow is halted by boundary resistance, and the tunnel has become completely blocked by sediment deposits (Figs. 15b and 16d). In Case C1, a clear-water flow layer solely exists in the reservoir and bottom tunnel, and the funnel-shaped bed morphology is stable, indicating that sediment flushing has been achieved (Fig. 15a).

Compared with the measured data and the empirical formulations of Xu et al. [25], the computed results of bed elevation for Case C1 (SF) are slightly different (Fig. 15a). By contrast, because the mechanism of pore water pressure is neglected in the present model, the computed results of bed elevation for Case C2 (TB) are roughly the same as the measured data (Fig. 15b). Overall, the present model successfully reproduces the occurrence of SF and TB under different conditions of cover layer thickness, and the computed results of bed elevation agree qualitatively with the measured data for the case of SF.

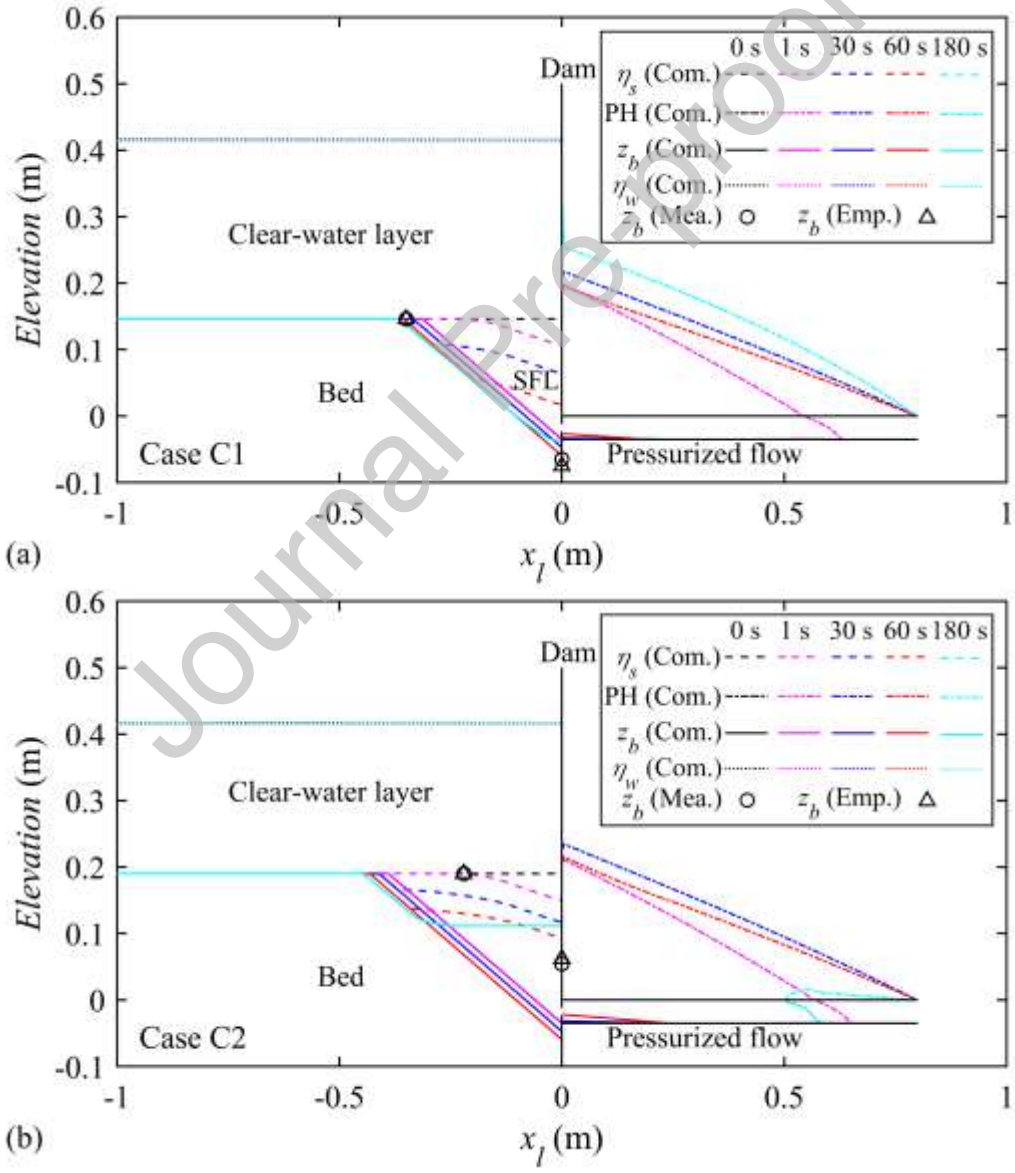

Fig. 15. (a) Case C1 and (b) Case C2, computed water surface η_w, interface η_s, piezometric

head (PH), and bed elevation z_b profiles along the central axis $y_l = 0\,\mathrm{m}$ at different times, as well as bed elevation from observation and the empirical formulations of Xu et al. [25], where SFL denotes sediment-laden flow layer.

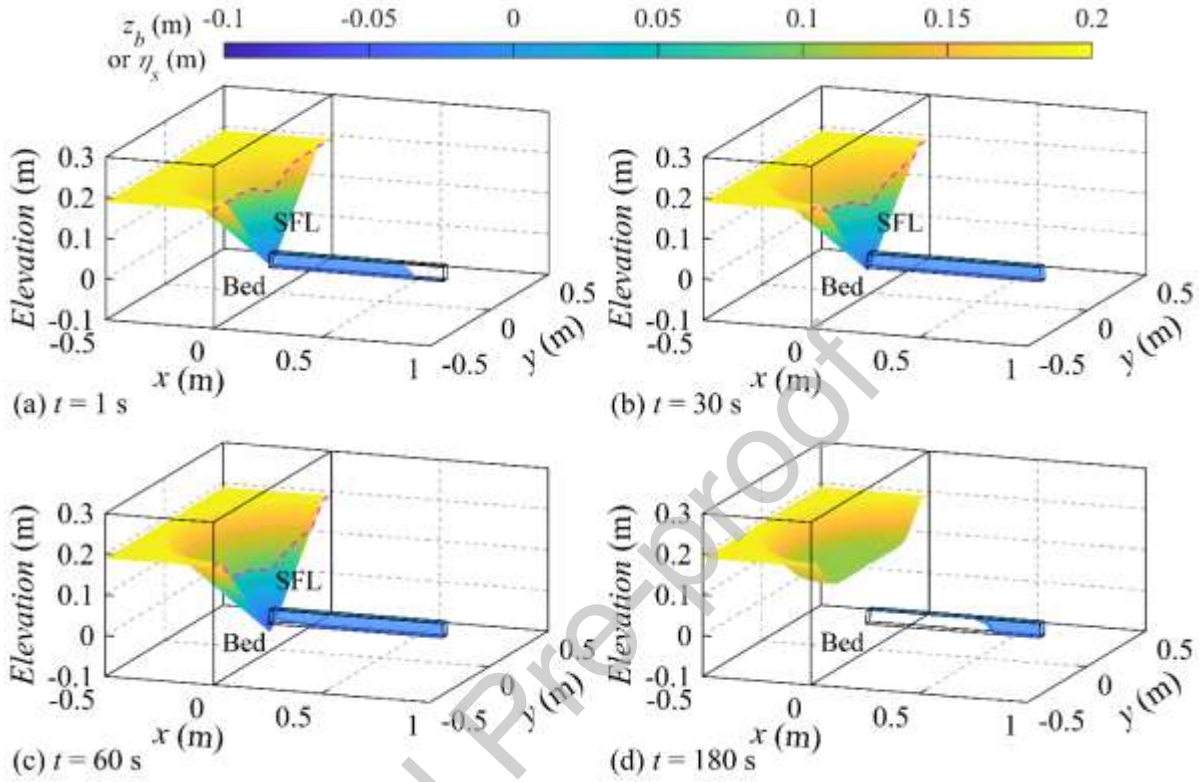

Fig. 16. Case C2, three-dimensional view of the upper surface of the sediment-laden flow layer η_s and bed z_b at times: (a) $t = 1\mathrm{s}$; (b) $t = 30\mathrm{s}$; (c) $t = 60\mathrm{s}$; and (d) $t = 180\mathrm{s}$.

Fig. 17 displays the bed shear stress τ_{eff} of sediment-laden flow layer in Cases C1 and C2 at four cross sections in the reservoir and tunnel. At each cross section, the bed shear stress diminishes over time. At the same time, the closer the sediment-laden flow layer is to the intake, the larger the bed shear stress τ_{eff} is in the reservoir, and the smaller the bed shear stress is in the tunnel. At $t = 60\,\mathrm{s}$, the bed shear stress at four cross sections in Case C1 (corresponding to a small cover layer thickness) is smaller than in Case C2. The pressure difference between the tunnel inlet and outlet is sufficient to overcome boundary resistance and drive the water-sediment mixture forward. This way, sediment flushing is accomplished

in Case C1. Thus, a smaller cover layer thickness h_{si} is beneficial to reservoir sediment flushing.

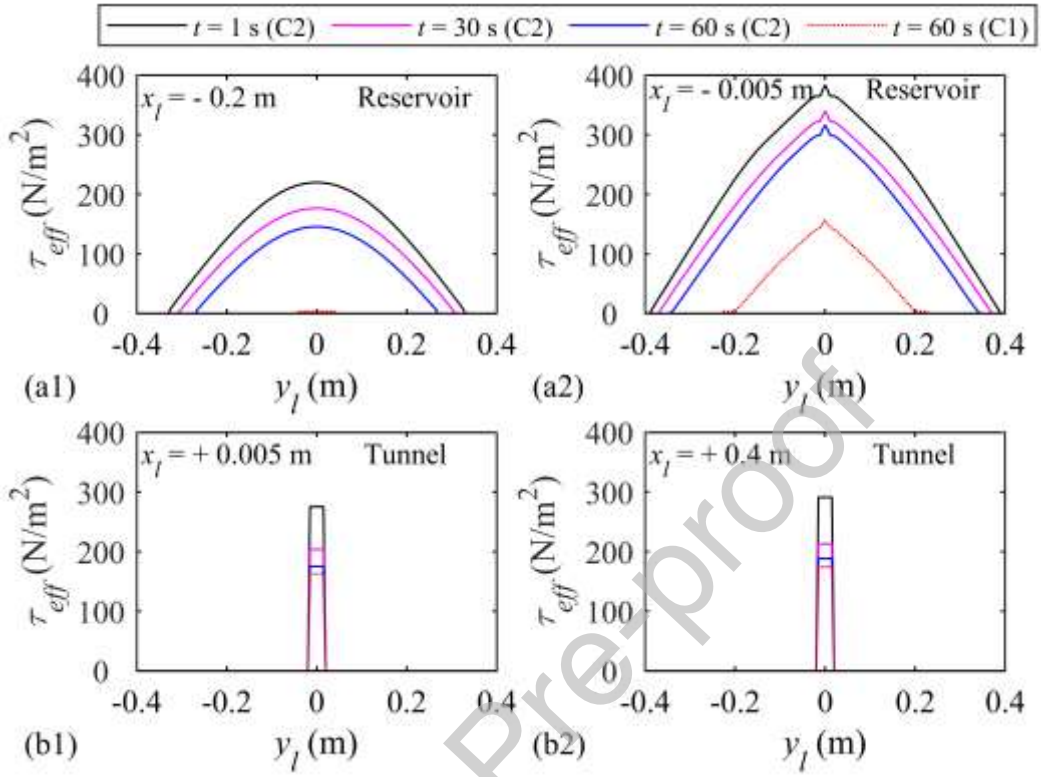

Fig. 17. Cases C1 and C2, bed shear stress τ_{eff} of the sediment-laden flow layer at different times at two cross sections upstream of the intake, (a1) $x_l = -0.2\,\mathrm{m}$, and (a2) $x_l = -0.005\,\mathrm{m}$, and two cross sections in the bottom tunnel, (b1) $x_l = +0.005\,\mathrm{m}$, and (b2) $x_l = +0.4\,\mathrm{m}$.

4.3.3 Effect of tunnel length and slope

The effect of tunnel types (i.e., length l_t and slope i_b) on the sediment flushing is demonstrated by comparing the computed results for Cases B2, D1 and D2. Alongside measured data and empirical formulations [25] for the equilibrium scour hole geometry, Fig. 18 presents the computed water surface elevation η_w, interface elevation η_s, piezometric head, and bed elevation z_b profiles along the central axis ($y_l = 0\,\mathrm{m}$) for Cases D1 and D2 at different times. As shown in Figs. 18a and 18b, the tunnel length l_t of Case D1 is

smaller than that of Case B2, while the bottom slope i_b of Case D2 is steeper than that of Case B2.

At $t = 1\,\mathrm{s}$, the front of the sediment-laden flow has reached the tunnel outlet in Case D1 (Fig. 18a) unlike Cases B2 and D2, where the front location in Case D2 is further downstream than in Case B2 (Figs. 18b and 12b). At $t = 15\,\mathrm{s}$, the funnel-shaped morphology formed by the interface between the two layers has deepened in the reservoir, and the bed layer in the reservoir has eroded without sediment deposition in the tunnel in both Cases D1 and D2 (Figs. 18a and 18b), in contrast to Case B2 which involves a longer tunnel of gentler slope (Fig. 12b). At $t = 30\,\mathrm{s}$, the lowest point of the interface in Case D1 is lower than the floor of the intake (Fig. 18a), whereas that in Case D2 is higher than the roof of the tunnel intake (Fig. 18b). In Case B2 the lowest point of the scour hole is much higher than the upper edge of the intake in the reservoir and the tunnel is blocked (Fig. 12b). Finally, at $t = 180\,\mathrm{s}$, both in Cases D1 and D2, a single-layer clear-water flow layer exists in the reservoir, and the outflow is almost clear water, confirming that reservoir sediment flushing has been accomplished. Meanwhile, the computed bed elevations at the upstream edge of the funnel-shaped scour hole of Cases D1 and D2 agree well with the measured data and the empirical formulations of Xu et al. [25] (Figs. 18a and 18b).

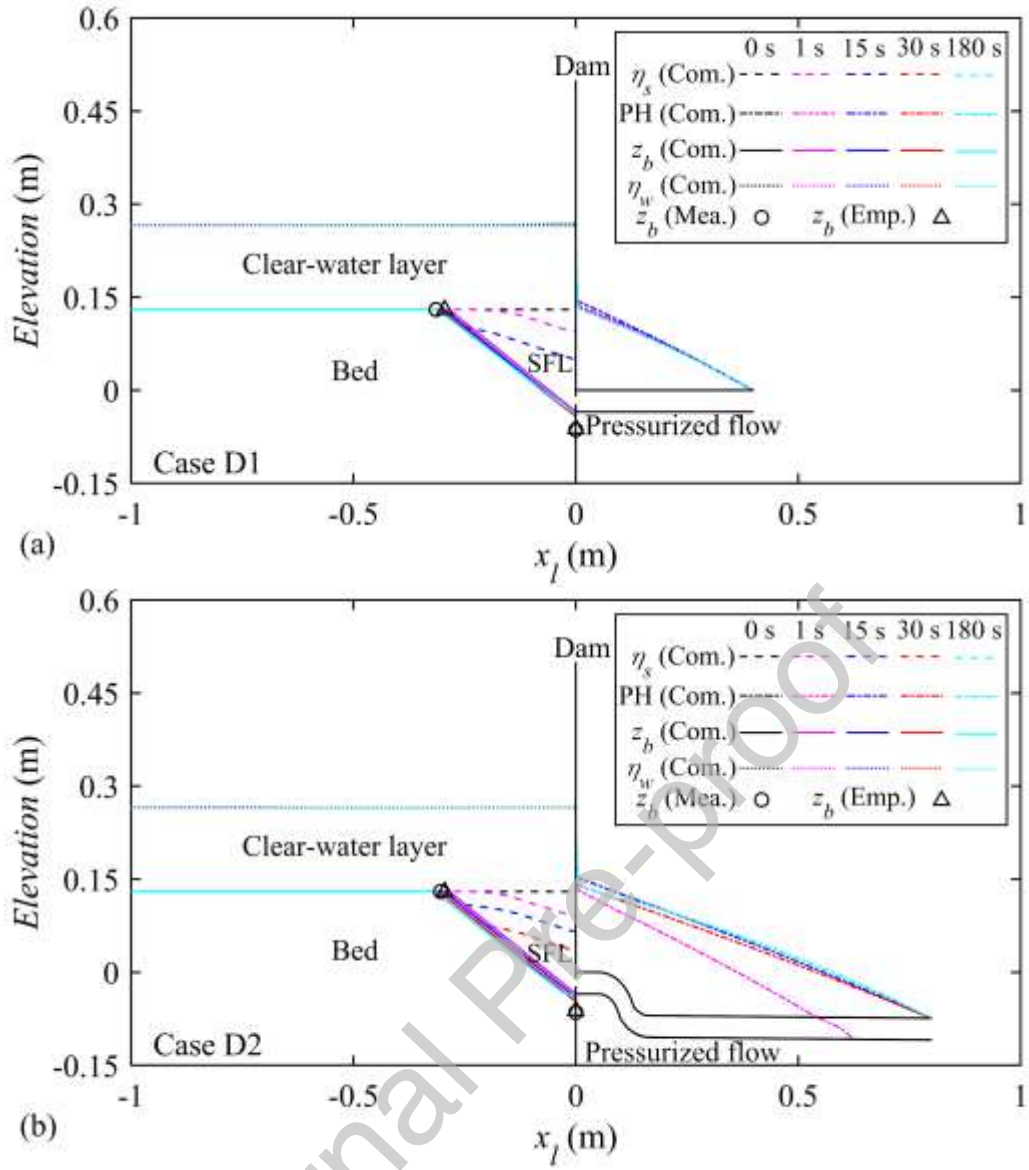

Fig. 18. (a) Case D1 and (b) Case D2, computed water surface η_w, interface η_s, piezometric head (PH), and bed elevation z_b profiles along the central axis $y_l = 0\,\mathrm{m}$ at different times, as well as bed elevation from observation and the empirical formulations of Xu et al. [25], where SFL denotes sediment-laden flow layer.

Fig. 19 displays transverse profiles of the bed shear stress τ_{eff} of the sediment-laden flow layer at four cross sections in the reservoir and tunnel for Cases B2, D1 and D2. At the cross sections $x_l = -0.2\,\mathrm{m}$ and $x_l = -0.005\,\mathrm{m}$, the bed shear stresses for Cases D1 and D2 gradually decrease over time in the reservoir as turbidity currents recede (see Figs. 19a1 and 19a2). At the cross sections $x_l = +0.005\,\mathrm{m}$ and $x_l = +0.4\,\mathrm{m}$, from $t = 1\,\mathrm{s}$ to 30 s, the

bed shear stress for Cases D1 and D2 decrease as the sediment concentration reduces in the tunnel (Figs. 19b1 and 19b2). Apparently, at $t = 15\,\mathrm{s}$, although the bed resistance for Case B2 is smaller at other cross sections, the bed resistance at $x_l = -0.005\,\mathrm{m}$ is larger than for Cases D1 and D2, leading to enhanced sediment deposition and bed aggradation near the intake, and hence TB. Thus, if the water level and cover layer thickness are held constant, the comparison between the results of Cases B2, D1, and D2 indicates that a shorter tunnel length or a steeper bottom slope is conducive to the occurrence of SF.

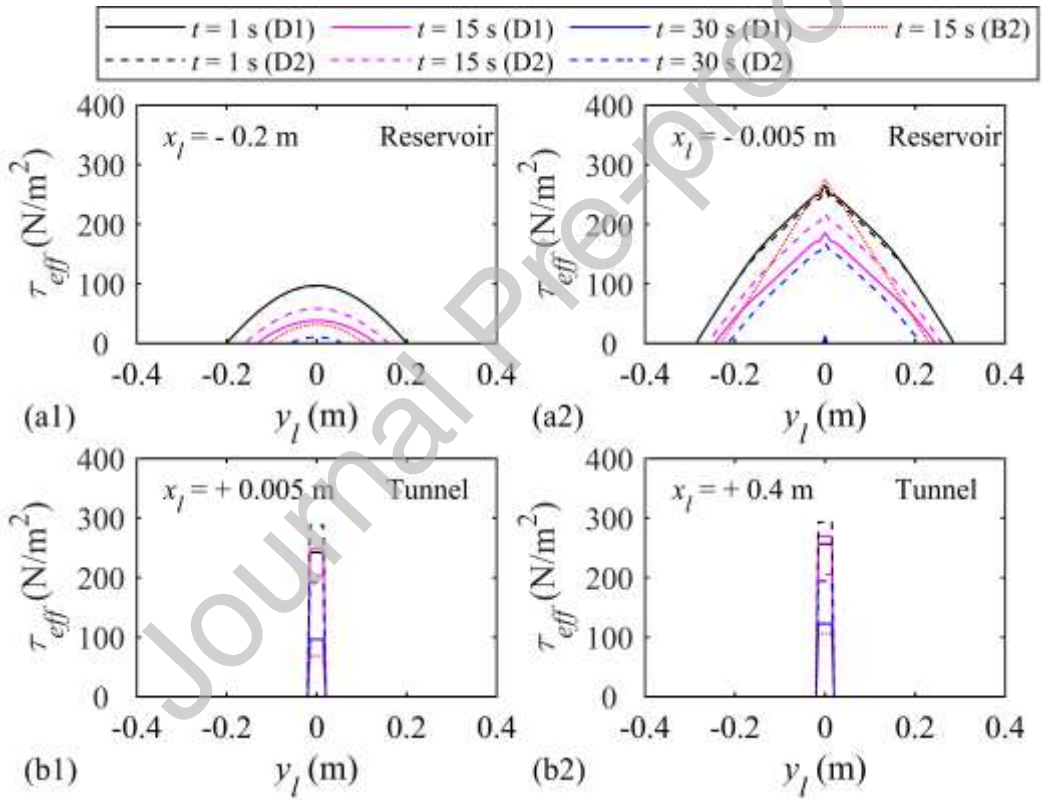

Fig. 19. Cases B2, D1 and D2, bed shear stress τ_{eff} of sediment-laden flow layer at different times at two cross sections upstream of the intake, (a1) $x_l = -0.2\,\mathrm{m}$, and (a2) $x_l = -0.005\,\mathrm{m}$, and two cross sections in the bottom tunnel, (b1) $x_l = +0.005\,\mathrm{m}$, and (b2) $x_l = +0.4\,\mathrm{m}$.

On the whole, if the water level in the reservoir is high, the cover layer thickness is low,

or the tunnel is short and its slope is steep, then the pressure difference between the inlet and outlet of the tunnel becomes sufficient to overcome boundary resistance and drive the water-sediment mixture along the tunnel to its outlet. A stable funnel-shaped scour hole then forms in the reservoir, and is symmetrical about the central axis of the tunnel intake. This way, higher reservoir water level, smaller cover layer thickness, and shorter tunnel length benefit the occurrence of reservoir sediment flushing. By contrast, if the water level is low, the cover layer thickness is large, or the tunnel is long and its slope is gentle, the smaller pressure difference between the inlet and outlet of the tunnel is insufficient to overcome the boundary resistance and the water-sediment mixture slowly propagates downstream. Sediment entering the tunnel cannot then be transported downstream, and ultimately, the bottom tunnel becomes completely blocked by sediment deposits.

5 Conclusions

The proposed model is the first of its kind to reproduce reservoir sediment flushing through a bottom tunnel with an initially covered intake, and couples a two-dimensional double layer-averaged model of the reservoir with a one-dimensional single layer-averaged model of the bottom tunnel. After validation against a series of flume experiments, further model simulations have provided insight into the influence of key factors (i.e., reservoir water level, cover layer thickness, and tunnel length and slope) on reservoir sediment flushing. The major findings are as follows:

(1) The proposed model successfully resolves the hydro-sediment-morphodynamic processes of reservoir sediment flushing in both the reservoir and bottom tunnel in

cases where the bottom tunnel (i.e., intake) is initially covered, and accurately predicts the occurrence of sediment flushing and tunnel blockage under different conditions.

(2) The computed results demonstrate that high reservoir water level, small cover layer thickness, short tunnel length and steep tunnel slope promote the occurrence of reservoir sediment flushing, in accordance with previous laboratory observations.

(3) The results prove that reservoir sediment flushing may be accomplished so long as the pressure difference between the inlet and outlet of the bottom tunnel suffices to overcome the boundary resistance of the hyper-concentrated sediment-laden flow. Factors that increase the pressure difference between the inlet and outlet of the tunnel (i.e., high reservoir water level and steep tunnel slope) and reduce boundary resistance (i.e., small cover layer thickness and short tunnel length) would therefore contribute to avoiding tunnel blockage.

The present study facilitates reservoir design and operation. To induce reservoir sediment flushing through a bottom tunnel with an initially covered intake, a short bottom tunnel with a steep slope should preferably be adopted in reservoir design, the cover layer thickness should be reduced by prompt desilting, and a high reservoir water level should be maintained.

It is noteworthy that the location and number of tunnel intakes also impact reservoir sediment flushing. Besides, the flushing process of non-cohesive sediment in this study is different from that of cohesive sediment [16, 53]. The foregoing requires further investigation through field observations and laboratory tests [54].

Acknowledgments

This work was funded by the National Natural Science Foundation of China under Grant No. 12072244.

References

[1] World Commission On Dams, Dams and development: A new framework for decision-making: The report of the world commission on dams, Earthscan Publications Ltd, London, 2000.

[2] W.R. White, Evacuation of sediments from reservoirs, Thomas Telford, London, 2001.

[3] J.H. Fan, Density currents and sedimentation engineering: Experiments and design, China Water & Power Press, Beijing, China, 2011. (in Chinese)

[4] A.J. Schleiss, M.J. Franca, C. Juez, and G. De Cesare, Reservoir sedimentation, J. J Hydraul Res. 54 (6) (2016) 595-614, doi: 10.1080/00221686.2016.1225320.

[5] S.A. Brandt, A review of reservoir desiltation, J. Int J Sediment Res. 15 (3) (2000) 321-342.

[6] S.M. Hajimirzaie, and R.H. Hotchkiss, Development of Sediment Management Guidelines for Small to Medium Reservoirs, J. J Hydraul Eng. 146 (12) (2020) 02520004, doi: 10.1061/(ASCE)HY.1943-7900.0001822.

[7] S. Ren, B. Zhang, W. Wang, Y. Yuan, and C. Guo, Sedimentation and its response to management strategies of the Three Gorges Reservoir, Yangtze River, China, J. Catena. 199 (2021) 105096, doi: 10.1016/j.catena.2020.105096.

[8] J. Fan, and G.L. Morris, Reservoir sedimentation II: Reservoir desiltation and long-term storage, J. J Hydraul Eng. 118 (3) (1992) 370-384, doi: 10.1061/(ASCE)0733-9429(1992)118:3(370).

[9] Z. Wang, and C. Hu, Strategies for managing reservoir sedimentation, J. Int J Sediment Res. 24 (4) (2009) 369-384, doi: 10.1016/S1001-6279(10)60011-X.

[10] G.L. Morris, Classification of management alternatives to combat reservoir sedimentation, J. Water-Sui. 12 (3) (2020) 861, doi: 10.3390/w12030861.

[11] G.M. Kondolf, Y. Gao, G.W. Annandale, G.L. Morris, E. Jiang, J. Zhang, Y. Cao, P.

Carling, K. Fu, Q. Guo, R. Hotchkiss, C. Peteuil, T. Sumi, H. Wang, Z. Wang, Z. Wei, B. Wu, C. Wu, and C.T. Yang, Sustainable sediment management in reservoirs and regulated rivers, J. Earth's Future. 2 (5) (2014) 256-280, doi: 10.1002/2013EF000184.

[12] J. Chen, W. Zhou, S. Han, and G. Sun, Influences of retrogressive erosion of reservoir on sedimentation of its downstream river channel—A case study on Sanmenxia Reservoir and the Lower Yellow River, J. Int J Sediment Res. 32 (3) (2017) 373-383, doi: 10.1016/j.ijsrc.2017.02.007.

[13] H. Wen Shen, Flushing sediment through reservoirs, J. J Hydraul Res. 37 (6) (1999) 743-757, doi: 10.1080/00221689909498509.

[14] G. Wang, B. Wu, and Z.Y. Wang, Sedimentation problems and management strategies of Sanmenxia Reservoir, Yellow River, China, J. Water Resour Res. 41 (9) (2005) W09417, doi: 10.1029/2004WR003919.

[15] D.N. Powell, and A.A. Khan, Scour upstream of a circular orifice under constant head, J. J Hydraul Res. 50 (1) (2012) 28-34, doi: 10.1080/00221686.2011.637821.

[16] S. Emamgholizadeh, and M. Fathi-Moghdam, Pressure flushing of cohesive sediment in large dam reservoirs, J. J Hydrol Eng. 19 (4) (2014) 674-681, doi: 10.1061/(ASCE)HE.1943-5584.0000859.

[17] H. Haghjouei, M. Rahimpour, K. Qaderi, and S.A. Kantoush, Experimental study on the effect of bottomless structure in front of a bottom outlet on a sediment flushing cone, J. Int J Sediment Res. 36 (3) (2021) 335-347, doi: 10.1016/j.ijsrc.2020.11.002.

[18] S. Guillen-Ludena, J.A. Toapaxi, and L.G. Castillo, Flushing capacity of a stored volume of water: an experimental study, J. Water-Sui. 14 (17) (2022), doi: 10.3390/w14172607.

[19] J.S. Lai, and F.J. Chang, Physical modelling of hydraulic desiltation in Tapu reservoir, J. Int J Sediment Res. 16 (3) (2001) 363-379.

[20] W.Y. Xue, W.X. Huai, Z.W. Li, Y.H. Zeng, Z.D. Qian, and Z.H. Yang, Numerical simulation of scouring funnel in front of bottom orifice, J. J Hydrodyn. 25 (3) (2013) 471-480, doi: 10.1016/S1001-6058(11)60386-8.

[21] D.N. Powell, and A.A. Khan, Flow field upstream of an orifice under fixed bed and

equilibrium scour conditions, J. J Hydraul Eng. 141 (2) (2015) 04014076, doi: 10.1061/(ASCE)HY.1943-7900.0000960.

[22] O. Sawadogo, G.R. Basson, and S. Schneiderbauer, Physical and coupled fully three-dimensional numerical modeling of pressurized bottom outlet flushing processes in reservoirs, J. Int J Sediment Res. 34 (5) (2019) 461-474, doi: 10.1016/j.ijsrc.2019.02.001.

[23] J. Huang, B. Greimann, and S. Kimbrel, Simulation of sediment flushing in Paonia reservoir of Colorado, J. J Hydraul Eng. 145 (12) (2019) 06019015, doi: 10.1061/(ASCE)HY.1943-7900.0001651.

[24] J. Liu, S. Minami, H. Otsuki, B. Liu, and K. Ashida, Prediction of concerted sediment flushing, J. J Hydraul Eng. 130 (11) (2004) 1089-1096, doi: 10.1061/(ASCE)0733-9429(2004)130:11(1089).

[25] H. Xu, Z.X. Cao, and Q. Wang, Experimental investigation on reservoir sediment flushing through a bottom tunnel with an initially covered intake, J. J Hydraul Eng. 149 (8) (2023) 04023024, doi: 10.1061/JHEND8.HYENG-13580.

[26] L. Guertault, B. Camenen, C. Peteuil, A. Paquier, and J.B. Faure, One-dimensional modeling of suspended sediment dynamics in dam reservoirs, J. J Hydraul Eng. 142 (10) (2016) 1-9, doi: 10.1061/(ASCE)HY.1943-7900.0001157.

[27] H.W. Wang, G.C. Yang, G.L. Morris, K.W. Chen, and Anonymous, Numerical study of sediment management strategies for Techi Reservoir in Taiwan, American Geophysical Union, Washington, DC, 2019.

[28] D.C. Hu, Studies on the three-dimensional numerical model for free-surface flow and suspended-sediment transport, Tsinghua University, Beijing, China, 2009, PhD thesis.

[29] Z.X. Cao, J. Li, G. Pender, and Q.Q. Liu, Whole-process modeling of reservoir turbidity currents by a double layer-averaged model, J. J Hydraul Eng. 141 (2) (2015) 04014069, doi: 10.1061/(ASCE)HY.1943-7900.0000951.

[30] Y.N. Sun, J. Li, Z.X. Cao, and A.G.L. Borthwick, A 2D double layer-averaged model of hyperconcentrated turbidity currents with non-Newtonian rheology, J. Int J Sediment Res. (2023) (accepted)

[31] J. Li, Z.X. Cao, and Q.Q. Liu, Waves and sediment transport due to granular landslides impacting reservoirs, J. Water Resour Res. 55 (1) (2019) 495-518, doi: 10.1029/2018WR023191.

[32] J. Li, Z.X. Cao, Y. Cui, X. Fan, W.J. Yang, W. Huang, and A.G.L. Borthwick, Hydro-sediment-morphodynamic processes of the baige landslide-induced barrier Lake, Jinsha River, China, J. J Hydrol. 596 (2021) 126-134, doi: 10.1016/j.jhydrol.2021.126134.

[33] J. Li, Z.X. Cao, Y. Cui, and A.G.L. Borthwick, Barrier lake formation due to landslide impacting a river: A numerical study using a double layer-averaged two-phase flow model, J. Appl Math Model. 80 (2020) 574-601, doi: 10.1016/j.apm.2019.11.031.

[34] Y. Jia, F. Zheng, H.R. Maier, A. Ostfeld, E. Creaco, D. Savic, J. Langeveld, and Z. Kapelan, Water quality modeling in sewer networks: Review and future research directions, J. Water Res. 202 (2021) 117419, doi: 10.1016/j.watres.2021.117419.

[35] M.J.S. Safari, M. Mohammadi, and A. Ab Ghani, Experimental studies of self-cleansing drainage system design: A review, J. Journal of Pipeline Systems. 9 (4) (2018), doi: 10.1061/(ASCE)PS.1949-1204.0000335.

[36] A. Campisano, C. Modica, E. Creaco, and G. Shahsavari, A model for non-uniform sediment transport induced by flushing in sewer channels, J. Water Res. 163 (2019) 114903, doi: 10.1016/j.watres.2019.114903.

[37] R.H.S.M. Shirazi, A. Campisano, C. Modica, and P. Willems, Modelling the erosive effects of sewer flushing using different sediment transport formulae, J. Water Sci Technol. 69 (6) (2014) 1198-1204, doi: 10.2166/wst.2013.810.

[38] A. Campisano, E. Creaco, and C. Modica, Numerical modelling of sediment bed aggradation in open rectangular drainage channels, J. Urban Water J. 10 (6) (2013) 365-376, doi: 10.1080/1573062X.2012.739627.

[39] W.M. Wu, Computational river dynamics, Taylor and Francis, London, 2007.

[40] J.X. Liu, Z.X. Cao, and X.C. Li, Coupled modelling of flow and non-capacity sediment transport in sewer flushing channel, J. Water Res. 219 (2022) 118557, doi: 10.1016/j.watres.2022.118557.

[41] Z. Cao, C. Xia, G. Pender, and Q. Liu, Shallow water hydro-sediment-morphodynamic equations for fluvial processes, J. J Hydraul Eng. 143 (5) (2017), doi: 10.1061/(ASCE)HY.1943-7900.0001281.

[42] J. Li, Z.X. Cao, K.H. Hu, G. Pender, and Q.Q. Liu, A depth-averaged two-phase model for debris flows over erodible beds, J. Earth Surf Proc Land. 43 (4) (2018) 817-839, doi: 10.1002/esp.4283.

[43] X.J. Fei, A model for calculating viscosity of sediment carrying flow in the middle and lower Yellow River, J. Journal of Sediment Research. 6 (2) (1991) 1-13, doi: 10.16239/j.cnki.0468-155x.1991.02.001. (in Chinese)

[44] G. Parker, Y. Fukushima, and H.M. Pantin, Self-accelerating turbidity currents, J. J Fluid Mech. 171 (3) (1986) 145-181, doi: 10.1017/S0022112086001404.

[45] J.F. Richardson, and W.N. Zaki, Sedimentation and fluidisation: Part 1, J. Chem Eng Res Des. 32 (1997) S82-S100, doi: 10.1016/S0263-8762(97)80006-8.

[46] E.F. Toro, Shock-capturing methods for free-surface shallow flows, Wiley, Chichester, U.K., 2001.

[47] P. Hu, A. Ji, W. Li, and Z. Cao, Numerical modelling of levee breach with an improved slope-failure operator, J. Journal of Hydraulic Research. (ahead-of-print) (2023) 1-13, doi: 10.1080/00221686.2023.2202661.

[48] J.G. Vasconcelos, and S.J. Wright, Comparison between the two-component pressure approach and current transient flow solvers, J. J Hydraul Res. 45 (2) (2007) 178-187, doi: 10.1080/00221686.2007.9521758.

[49] F. Aureli, S. Dazzi, A. Maranzoni, and P. Mignosa, Validation of single- and two-equation models for transient mixed flows: a laboratory test case, J. J Hydraul Res. 53 (4) (2015) 440-451, doi: 10.1080/00221686.2015.1038324.

[50] J.X. Liu, Z.X. Cao, X.C. Li, W.J. Wang, J.M. Hou, D.L. Li, and Y. Ma, Modelling urban flooding integrated with flow and sediment transport in drainage networks, J. Sci Total Environ. 850 (2022) 158027, doi: 10.1016/j.scitotenv.2022.158027.

[51] J.M. Hou, F. Simons, M. Mahgoub, and R. Hinkelmann, A robust well-balanced model on unstructured grids for shallow water flows with wetting and drying over complex

topography, J. Comput Method Appl M. 257 (2013) 126-149, doi: 10.1016/j.cma.2013.01.015.

[52] H.V. Gupta, S. Sorooshian, and P.O. Yapo, Status of automatic calibration for hydrologic models: comparison with multilevel expert calibration, J. J Hydrol Eng. 4 (2) (1999) 135-143, doi: 10.1061/(ASCE)1084-0699(1999)4:2(135).

[53] A. Campisano, E. Creaco, and C. Modica, Laboratory investigation on the effects of flushes on cohesive sediment beds, J. Urban Water J. 5 (1) (2008) 3-14, doi: 10.1080/15730620701726259.

[54] J. Bertrand-Krajewski, A. Campisano, E. Creaco, and C. Modica, Experimental analysis of the Hydrass flushing gate and field validation of flush propagation modelling, J. Water Sci Technol. 51 (2) (2005) 129-137, doi: 10.2166/wst.2005.0040.

Declaration of interests

☑ The authors declare that they have no known competing financial interests or personal relationships that could have appeared to influence the work reported in this paper.

☐The authors declare the following financial interests/personal relationships which may be considered as potential competing interests: